PHYSICAL REVIEW B **89**, 035424 (2014)

Kondo effect of a cobalt adatom on a zigzag graphene nanoribbon

Damian Krychowski, Jakub Kaczkowski, and Stanislaw Lipinski[*]
Institute of Molecular Physics, Polish Academy of Sciences, M. Smoluchowskiego 17, 60-179 Poznań, Poland

(Received 22 July 2013; revised manuscript received 12 December 2013; published 21 January 2014)

Based on *ab initio* calculations we discuss the Kondo effect due to a Co adatom on a graphene zigzag nanoribbon. A Co atom located at a hollow site behaves as a spin $\mathcal{S} = 1/2$ impurity with d_{xz} and d_{yz} orbitals contributing to the magnetic moment. Dynamical correlations are analyzed with the use of complementary approximations: the mean field slave boson approach, noncrossing approximation, and equation-of-motion method. The impact of interplay between spin and orbital degrees of freedom together with the effect of peculiarities of electronic and magnetic structure of the nanoribbon on many-body resonances is examined.

DOI: 10.1103/PhysRevB.89.035424 PACS number(s): 73.22.Pr, 73.23.−b, 75.20.Hr, 85.75.−d

I. INTRODUCTION

Graphene possesses spectacular electronic, optical, magnetic, thermal, and mechanical properties, which make it an exciting material for technological applications [1–5]. Graphene is a semimetal. For use in logic devices a controllable band gap is very much desired. The presence of a gap would increase tremendously the on-off ratio for current flow that is needed for many electronic applications. For example, lack of the gap prevents the use of graphene in making transistors. A band gap opening is caused by symmetry breaking [6,7]. The most effective way within the realm of single-layer graphene physics is electron confinement, e.g., in nanoribbons (partial breaking of translational symmetry) [8–11]. The graphene nanoribbons (GNRs) with varying widths can be realized either by cutting [12] mechanically exfoliated graphenes [13] or by pattering epitaxially grown graphenes [14]. The edge geometry is the key factor which determines the electronic properties of the nanoribbon. There are two types of nanoribbons, based on their edges shapes, called zigzag (ZGNR) and armchair (AGNR) [9,15]. Recently, electronic devices, such as field effect transistors, have been formed from graphene nanoribbons [16,17]. ZGNRs are of particular interest, because due to topological reasons they are forming edge states [18], i.e., states decaying exponentially into the center of the ribbon [3,19]. The decay lengths are in the range of a few nanometers [20]. The edge states have been observed in scanning tunneling microscopy [21]. The localized nature of these states gives rise to a flat band extending over one-third of the one-dimensional Brillouin zone and correspondingly also to a sharp peak in the density of states right at the Fermi level. As a consequence a magnetic ground state emerges from a Fermi instability [22,23]. Recently the spin splitting of the edge density of states of ZGNRs has been confirmed experimentally [24]. Theoretical studies have shown that the spins on each edge are ferromagnetically ordered, and those between the edges are antiferromagnetically coupled, the latter resulting from the interaction of the tails of the edge states [10,23,25–27]. Modification of the electronic structure can be also introduced by chemical functionalization, which allows the band gap engineering and designing different types of magnetic order. Based on density functional calculations (DFT) Son *et al.* [22] have shown that one can modify the band gap of ZGNRs by applying transverse electric field and that the electric field closes the gap for one of the directions selectively (half metallicity). This conclusion has been confirmed by calculations of Kan *et al.* [27] with the use of a hybrid functional potential (B3LYP), which is viewed as one of the most accurate methods for estimation of the gap. The predicted critical fields of transition into half metallicity are much higher in this method than those from normal DFT calculations. It is well known that graphene nanostructures are promising for spintronics due to their long spin relaxation and decoherence times owing to the low intrinsic spin-orbit interaction [28]. The mentioned possibility of band gap tuning and controlling magnetism and spin transport of the ribbons by electric field is the principal advantage of these systems. The pure nanoribbon has no net magnetic moment. The functionalities of the ribbons can be enriched by doping the magnetic adatoms. Due to the open surface controlled adatoms manipulation is within reach of atomic force microscopy in these systems [29,30]. In the last few years several studies focused on understanding structural, electronic, and magnetic properties of 3*d* impurities in graphene nanoribbons [31–36]. Also vacancies and defects have been predicted to give rise to magnetic moments [37,38]. The relative stability of local moments depends on the balance between the Coulomb repulsion, exchange interaction, position of 3*d* levels, and hybridization with the neighboring carbon atoms. Especially the two latter factors are strongly affected by impurity location: one expects different energetics, structural, and electronic properties near the edge sites of GNRs and different when the adatom is located inside the ribbon. The electronic structure of a nanometer-wide ribbon is dominated by confinement effects and Van Hove singularities and this strongly affects the hybridization path. As opposed to normal metals, the damping of the local levels is energy dependent and the hybridization self-energy acquires also significant real contribution near singularities causing effective shift of local energy levels. Since the chemical potential of GNRs can be tuned, a formation of local moment can be controlled by gate voltage and particularly strong gate dependence is expected near singularities. At low temperature, the localized spin is screened by conduction electrons and a narrow Kondo peak appears near the Fermi level. Most of the early studies on the Kondo effect were carried on for metallic systems with constant density of states at the Fermi surface; in the case of graphene structures the details of the band structure play the decisive role in screening. Recently the Kondo effect has been observed in graphene both in resistivity

---

[*] lipinski@ifmpan.poznan.pl

1098-0121/2014/89(3)/035424(20)

measurements [39] and by scanning tunneling microscopy (STM) [40]. As opposed to transport measurements STM probes local electronic properties of Kondo impurities. The Kondo resonance observed in tunneling spectroscopy usually does not show up as a peak but rather as a dip. This is a consequence of interference of the direct channel into the localized orbitals of the impurity and an indirect one to the bands of the host [41]. The Kondo temperature in graphene is tunable with carrier density from 15–90 K [39,40]. A number of interesting theoretical studies have been published on this topic discussing specificity of Kondo screening for the gapless system, where a critical hybridization is necessary for the occurrence of this effect [42–44]. Due to valley degeneracy of the Dirac electrons in perfect graphene the possibility of a multichannel Kondo effect has been also discussed [45]. Recently there appeared two fundamental, realistic studies of the Kondo effect of a single Co adatom in graphene based on first-principles calculations [46,47]. These papers expose the role of orbital symmetry on dynamical correlations. Along this line is also the analysis presented in the present paper.

The topic of our study is the Kondo effect in a zigzag graphene nanoribbon. The crucial requirement of the occurrence of the Kondo effect is that the adatom should retain its magnetic moment in the presence of electrons of the host. We open our analysis with presentation of the first-principles electronic structure calculations of the Co impurity in narrow zigzag GNRs discussing energetics, geometry of adsorption, magnetic moments, and magnetization densities for different positions of impurities. We discuss which adsorption site is most favorable and show the result of optimization of the adsorption height, and indicate which orbitals most strongly hybridize with nanoribbon states and which contribute to impurity magnetic moments. Both the binding energies of the impurity and the magnitude of the moment strongly depend on the location of the adatom across a ribbon. Due to the strong variation of the ZGNR density of states with chemical potential an interesting question arises of the possibility of driving the magnetic impurity in and out of the Kondo regime. Another important problem is how the Kondo screening is affected by ZGNR edge states and what is the role of polarization of these states in the spin-orbital Kondo effect. Performing the calculations for different locations of the chemical potential with respect to the band gap, also for the case when it crosses the low-energy singularities of density of states, allows us to analyze different coupling regimes and track the impact of symmetry breaking in both orbital and spin sectors. In general more than one orbital effectively contribute to the magnetic moment and in the Kondo screening apart from spin also orbital degrees of freedom are involved. The role of the orbital of a given symmetry changes both with geometrical location of impurity and with position of the Fermi level. Static mean field methods such as density functional calculations (DFT) cannot describe dynamical electron correlations. Therefore for simple and intuitive analysis of many-body correlations we use the multiorbital Anderson-like model in which the impurity is described by parameters but the nanoribbon electronic structure and hybridization function are calculated within DFT. This Hamiltonian is then solved in the next step by commonly used many-body approximate methods with the well-known applicability regimes and limitations. The principal method used in the present work, the slave boson mean field approach (SBMFA), best describes systems close to the Kondo fixed point, i.e., for the case of fully degenerate deep atomic levels at low temperatures [48], but often is also used for a qualitative insight away from this limit. We adopt the Kotliar-Ruckenstein formulation [49,50], which is a convenient tool for discussing the finite Coulomb interaction case and for analysis of effects introduced by polarization. Two other complementary methods used by us - the equation-of-motion method (EOM) [51–54] and the noncrossing approximation (NCA) [55–60] - allow us to get a deeper insight into the role of charge fluctuations in many-body physics and are better adopted for higher temperatures. EOM works in the whole parameter space except the close vicinity of the Kondo fixed point but it breaks at low temperatures [53] and NCA gives reliable results in the wide temperature range, including the region close to T_K and in the range of the lowest temperatures down to a fraction of T_K. It is claimed that this method is not suitable for spin-polarized systems due to the well-known artifacts resulting from the neglect of vertex corrections [54].

The paper is organized as follows: Section II presents density functional theory calculations of electronic and magnetic properties of zigzag graphene nanoribbons and analyzes adsorption of the Co adatom in these structures. In Sec. III the generalized Anderson model with DFT hybridization function is described. Next we present numerical results and analyze the impact of confinement and band gap singularities of electronic structure as well as the role of orbital physics and magnetic polarization on the Kondo effect. Finally, we give conclusions and some final remarks in Sec. IV.

II. DENSITY FUNCTIONAL STUDY OF Co ADATOM ON ZGNR

A. Computational details

Zigzag nanoribbons are quasi-one-dimensional structures with infinite length and nanometric widths, the latter being defined by the parameter N indicating the number of zigzag lines along the ribbon widths. Most of our considerations are addressed to 4ZGNR ($N = 4$, Fig. 1), but we also present some comparative calculations for wider ribbons. To saturate the edge C dangling bonds the ribbons are passivated by hydrogen atoms. The following first-principles analysis of Co adatoms on graphene nanoribbons provides the necessary input information for analysis of correlation effects, which we undertake in the next section. Here we discuss which are the most favorable adsorption sites for the Co atom, the corresponding electron configurations and magnetic moments, as well as impurity-induced magnetic polarization of the ribbon. For simulation of Co impurity we have used a supercell consisting of four graphene unit cells, which contains one adatom. To check whether this supercell is sufficiently large to obtain reliable results, especially concerning magnetic moment, we have also performed testing calculations for larger supercells, obtaining similar results. We consider three classes of high-symmetry adsorption sites presented in Fig. 1: hollow, in the center of the carbon hexagon (h); top, at the carbon atom (t); and bridge (b), between two carbon atoms. Unlike graphene, where an infinite plane ensure the equivalence of lattice sites, in nanoribbons the number of inequivalent

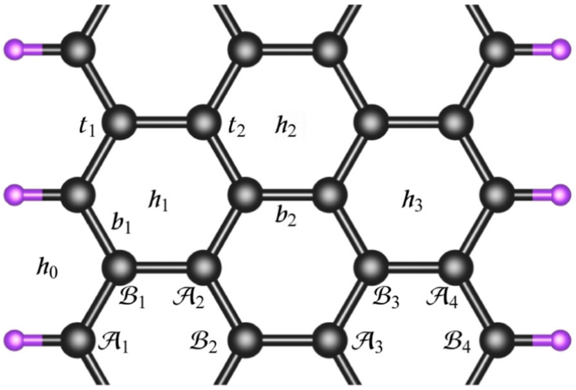

FIG. 1. (Color online) Structure of H-passivated 4ZGNR, where the dark gray and purple/light gray spheres represent the C and H atoms, respectively. Labeling of carbon atoms across the ribbon with division into sublattices is introduced. The possible adatom locations h_1, h_2, h_3 (hollow positions, most favorable); t_1, t_2: top sites; b_1, b_2: bridge positions; and perturbed hollow-like site of the edge h_0 are depicted.

position of impurities within each class increases with the width of the ribbon. For convenience of the discussion the different carbon atoms spaced across the ribbon are also marked in Fig. 1. To get an insight into the interaction of Co adatoms on nanoribbons we performed spin-polarized density functional calculations. The main idea of DFT is to describe the interacting system of fermions via its density and not via its many-body wave function [61]. The key problem of DFT formalism is a choice of exchange-correlation potential. Most of our calculations have been performed using the semilocal generalized gradient approximation (GGA) with the Perdew, Burke, and Ernzerhof (PBE) formula for the exchange correlation [62]. The inclusion of gradient corrections is of special importance for the considered systems, because large gradients in the charge density occur at the nanoribbon edges. Since it is known that local approaches often underestimate magnetic moments and band gaps, we have also done some test calculations using the hybrid nonlocal exchange potential HSE [63–68]. The mixing of nonlocal and semilocal exchange overcomes the major flaws of LDA or GGA [10,69]. Concerning the choice of the wave function basis set, two codes have been employed: the Vienna simulation package (VASP) [70] with the projector augmented wave basis sets (PAW) [71], and OPENMX, which uses basis sets of localized pseudoatomic orbitals (LCPAOs) [72]. In the latter case for the geometrical optimization and the electronic band structure calculations the LCPAO basis functions were specified by the choice of two primitive orbitals for s component and one primitive orbital for p component for hydrogen (H5.0-$s2p1$) and three p orbitals for carbon (C5.0-$s2p3$). The cutoff radius of 5.0 bohrs has been assumed. The VASP code is widely used, but due to the plane wave picture it is difficult to describe the effects of edges and to discuss field-induced charge accumulation or dipole moments. In both codes the GGA-PBE exchange-correlation potential has been adopted [62], which is specified not only by spin densities, but also by their gradients. In comparison with LSD, GGA's tend to improve total energies and structural difference [62]. In VASP, where smooth pseudopotentials are used, a kinetic energy cutoff of 400 eV was found to be sufficient to achieve a total energy convergence of the energies of the systems to within 1 meV. In OPENMX a real-space grid technique was adopted in numerical integration with energy cutoff up to 150 Ry. In both methods the structures were relaxed until the Hellman-Feynman force became smaller than 10^{-4} Ha/bohr. Brillouin integration was carried out at an $8 \times 1 \times 1$ Monkhorst-Pack grid and Gaussian smearing of 0.03 eV was chosen to accelerate electronic convergence in both codes. For band structure calculations 50 and 200 uniform k points along the one-dimensional BZ were used in VASP and OPENMX, respectively. To avoid interaction between images made by periodic boundary conditions the vacuum region was set up to 18 Å in the y direction and up to 20 Å in the z direction; in the x direction the ribbon was treated as infinite. The adatom-ribbon system lacks inversion symmetry and therefore has a net electric magnetic moment perpendicular to the surface. To remove spurious dipole interaction between periodic images, we self-consistently applied corrections to the local electrostatic potential and total energy [73]. To test the impact of correlations on the adsorption energy and magnetic moments we have performed also some GGA+U type calculations using the rotationally invariant LDA+U functional proposed by Lichtenstein *et al.* [74]. The stability of the adatom on the relaxed GNR was examined analyzing adsorption energy defined as

$$\mathcal{E}_{\mathrm{ads}} = \mathcal{E}_{\mathrm{ZGNR+Co}} - \mathcal{E}_{\mathrm{ZGNR}} - \mathcal{E}_{\mathrm{Co}}, \tag{1}$$

where the first term is total energy of ZGNR with Co adatom, and the second and third are total energies of clean ZGNR and isolated Co atom.

B. Electronic and magnetic properties of ZGNR

It is now well established that the zigzag edge GNR is a semiconductor with two electronic edge states, which are ferromagnetically (F) ordered, but antiferromagnetically (AF) coupled to each other [22,25,27]. This configuration is consistent with the Lieb theorem [75]. It is also well understood that magnetism of the edges arises from a Fermi instability of the edges [65]. Our VASP calculations show that for $N = 4$ the unpolarized solution has energy by $\Delta\mathcal{E} = 55.74$ meV per edge carbon atom higher compared to the AF state and 13.23 meV higher than the F state. The energy difference between parallel and antiparallel orientations of magnetizations at the edges decreases with the width (Table I) indicating that the increase of the overlap of edge states is responsible for relative ordering of polarizations. The obtained values are in good agreement with results reported by other groups [78–82].

Figure 2 compares spin density plots of 4ZGNR calculated with the local exchange potential (GGA-PBE) with the corresponding picture obtained within the nonlocal approach (HSE). Estimation of magnetic moment is sensitive to the choice of exchange potential; for the nonlocal functional HSE [Fig. 2(b)], much higher values are obtained and slower decay towards the center of the ribbon. These trends can be understood as a consequence of the well-known property of nonlocal potentials, which localize electronic states more strongly compared to local potentials [63,64]. It is clearly

TABLE I. Differences between energies of NZGNR states with antiparallel (AF) and parallel (F) alignment of magnetic moments on the left and right edges compared with corresponding differences of energies of AF and nonmagnetic states ($N = 3$–10) (VASP).

N	$\mathcal{E}_{AF-F}$ (meV)	$\mathcal{E}_{AF-NM}$ (meV)
3	−18.61	−39.01
4	−13.23 (−14[a], -15[b], −11[c])	−55.74 (−59[a])
5	−10.67	−65.10
6	−11.39 (−11.9[d], −15[a])	−69.41 (−85.7[d], −81[a])
7	−8.83 (−11.2[d])	−71.64 (−89.4[d])
8	−5.88 (−8.4[d], −7[a])	−73.73 (−91.8[d], −83[a])
9	−4.23	−75.75
10	−3.34 (−5.5[e])	−77.47

[a] Quantum-Espresso, PBE, Ref. [78].
[b] VASP, PBE, Ref. [79].
[c] SIESTA, PBE, Ref. [80].
[d] SIESTA, PBE, Ref. [81].
[e] SIESTA, PBE, Ref. [82].

seen that spin moments are mainly distributed at the edge carbon atoms. The magnetic moment fluctuation across the ribbon arises from quantum interference effects caused by edges. Due to topology of the lattice, the atoms of the two edges belong to different sublattices of the bipartite graphene lattice. The spin moments on the C atoms on one edge are antialigned to the spin moments on the opposite edge and also the polarizations of neighboring sites belonging to different sublattices are opposite. Figures 3(a) and 3(b) present 4ZGNR bands calculated with the VASP code decorated with local spin dependent edge contributions (overlap of the band eigenstates with p_z state localized at $\mathcal{A}_1$). Two observations are striking, first that the top of the valence band and the bottom of the conduction band are composed mainly of edge states, especially close to the zone boundary, and second, that in momentum range $2\pi/3a < k < \pi/a$ (a is ZGNR lattice constant) the lowest unoccupied conduction band (LUCB) and the highest occupied valence band (HOVB) are characterized by opposite spin polarizations. Of course for the right edge ($\mathcal{B}_4$) the spin contributions change roles. We have put also on Fig. 3(a) bands calculated by the OPENMX code. As one can expect, substantial differences between dispersion curves from both codes are only visible for small wave vectors, where VASP calculations should be superior due to the plane wave basis set. We have also marked in Fig. 3(a) the direct band gap (Δ_0) and the energy gap at the zone boundary (Δ_1). The magnetization-induced staggered potential opens a band gap. The direct band gap decreases with the increase of the width of the ribbon due to confinement and decrease of edge spin polarization [Fig. 3(c)]. The energy gap at the zone boundary on the other hand is almost not sensitive to the width, because as stated earlier, the edge states close to the zone boundary are highly confined at the edge of ZGNR. The direct band gaps calculated by both codes differ only slightly; in VASP they are smaller due to the deeper minimum in the lowest conduction band, which in turn again is a consequence of more extended character of VASP basis set. It is known that local or semilocal approximations such as GGA routinely underestimate semiconductor band gaps, due to self-interaction errors [64]. For comparison we have also calculated the band gap with the HSE potential; the obtained value is surprisingly high ($\Delta_{\mathrm{HSE}} = 1.58$ eV for 4ZGNR), but agrees with other HSE calculations [76]. It is generally accepted that band gaps obtained using hybrid functionals are in much better agreement with experimental data, although overestimated [68,77].

C. Co adatom

The computational tools we use (VASP, OPENMX) are developed for periodic structures and therefore we simulate the single-impurity problem by superstructure calculations. As a consequence of periodicity the extra features in the generated band structure can occur, e.g., additional gaps, not related to finite geometry, but to the assumed superstructure. It is believed, however, that using large enough supercells one can still infer some single-impurity properties. This concerns mainly quantities which depend on the entire density of states and not just on the behavior near the Fermi level, e.g., occupations or magnetic moments. With some caution one can get also an insight into some parts of the electronic structure, where superstructure does not interfere considerably. In our study we use a supercell consisting of four replicas of the ZGNR unit cell (4 × 1). This setup corresponds to a coverage of 1 adatom per 32 C atoms. Although the adatom-adatom interaction is not very small, the distance between adatoms is large enough that the overlap of the electronic states of neighboring atoms is negligible. Several test simulations were also carried out for

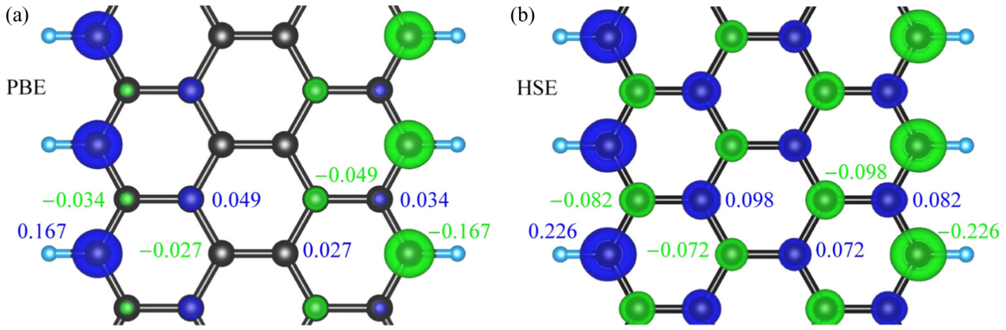

FIG. 2. (Color online) Spin density plots of 4ZGNR showing up (blue/dark gray) and down (green/light gray) spin densities together with the corresponding values of local magnetic moments calculated with VASP code using (a) GGA-PBE exchange correlation potential and (b) nonlocal GGA-HSE potential.

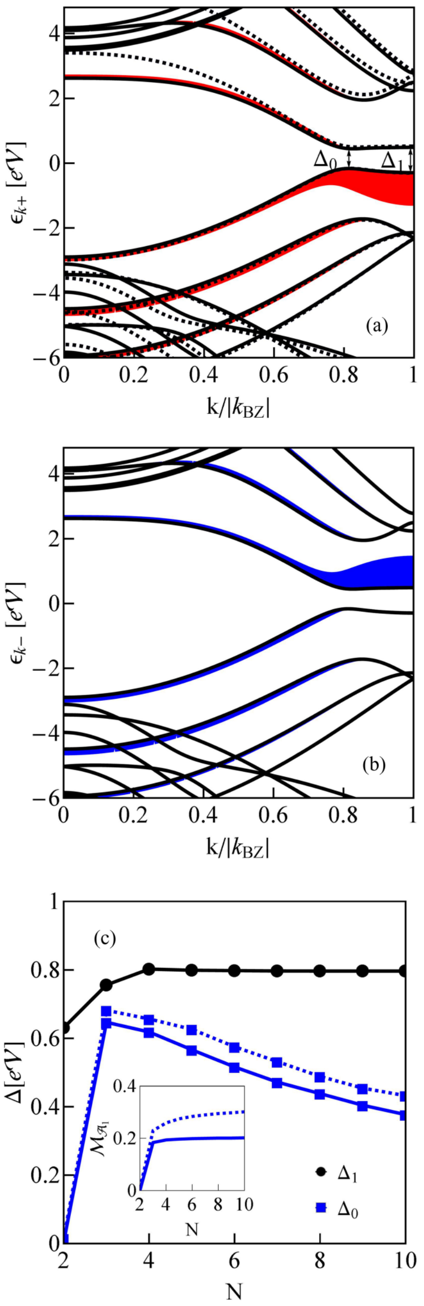

FIG. 3. (Color online) (a), (b) VASP spin-degenerate bands of 4ZGNR with *fat bands* showing the amplitudes of the projection of each band on p_z orbital of edge atom $\mathcal{A}_1$. Broken lines represent dispersions calculated by OPENMX code. Δ_0 and Δ_1 are direct band gap and gap of the zone boundary. (c) Width dependence of the nanoribbon gaps. Inset shows the width dependence of edge magnetic moments (solid line, VASP; broken line, OPENMX).

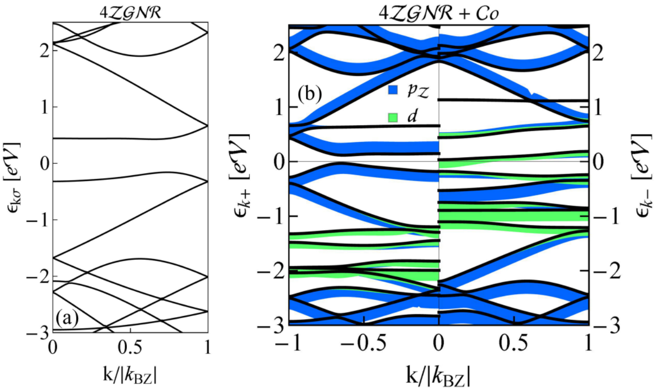

FIG. 4. (Color online) VASP energy dispersion curves of 4ZGNR (a) compared with the bands of 4ZGNR with Co impurity in h_1 position (b). The blue/dark gray fat bands highlight carbon p_z contribution and green/light gray the Co d contribution.

an 8×1 supercell. Periodic boundary conditions were also used along the confined direction assuming 20 Å of vacuum to prevent unphysical interactions. Different positions, as indicated in Fig. 1, were sampled. Figure 4 presents an example of the band structure of the 4ZGNR+Co system with the adatom in the h_1 position compared with the band structure of pure nanoribbons. The bands are decorated by the amplitudes of projection on atomic p_z orbitals of carbon and Co d orbitals. The strong interaction between cobalt and carbon atoms comes from the mixture of these states. Carbon p_x and p_y orbitals are far below $\mathcal{E}_{\mathcal{F}}$ and have weak hybridization with cobalt. Figure 5 displays spin- and orbital-resolved Co adatom densities of states. Both the in-plane orbitals (xy, $x^2 - y^2$) and xz, yz orbitals strongly hybridize with carbon p_z states, which results in covalent interactions. Densities of states of z^2 symmetry ($3z^2 - r^2$) for hollow positions show localized peaks, which indicate small overlap and hybridization with p_z. For Co location closer to carbon sites, e.g., for h_0 position (distance to B_1 is by 0.45 Å smaller than for h_1), hybridization of the d_{z^2} orbital increases and broadening of the corresponding peaks is observed [compare the insets of Fig. 5(d)]. For

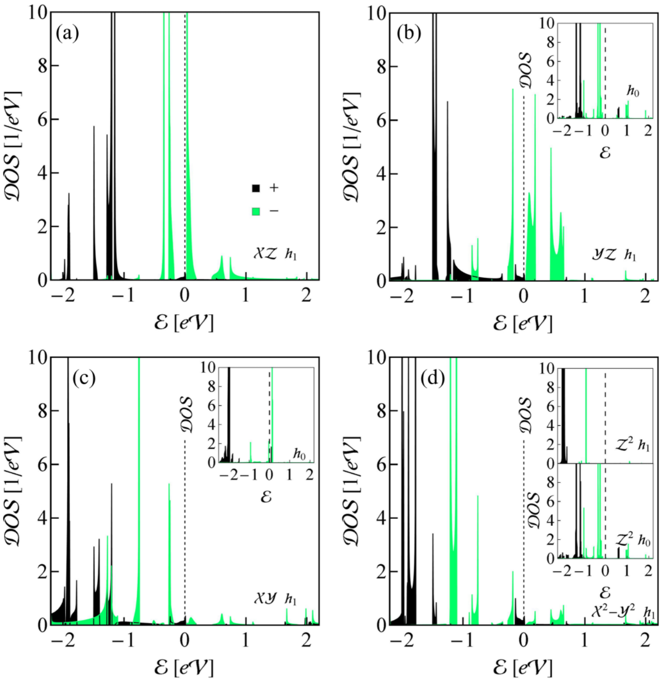

FIG. 5. (Color online) Spin- and orbital-resolved densities of states of Co adatom at h_1 position in 4ZGNR. Black denotes spin-up contributions and green/light gray the spin-down contributions. Insets of (b) and (c) present yz and xy partial DOS of Co adatom at h_0 site and insets of (d) compare z^2 partial DOS in h_1 and h_0 positions.

TABLE II. Equilibrium heights above nanoribbon plane and adsorption energies of Co adatom at different positions of 4ZGNR (VASP with GGA-PBE).

	h_{eq} (Å)	$\mathcal{E}_{\mathrm{ads}}$ (eV)
h_0	1.7	−1.261
h_1	1.53	−1.396
h_2	1.53	−1.258
t_1	1.83	−0.341
t_2	1.85	−0.407
b_1	1.79	−0.946
b_2	1.85	−0.477

Co at h_1, the bonding, almost completely occupied orbitals $d_{x^2-y^2}$, d_{xy} lie lower in energy than d_{xz} and d_{yz}; the latter are partially filled and they play an active role in formation of magnetic moment. Depending on the position of the adatom some orbitals may swap roles. This can be seen comparing for example the d_{xy}, d_{yz} partial DOS for h_1 and h_0 sites [Figs. 5(b) and 5(c)]. For the h_0 position the d_{yz} orbital becomes fully occupied whereas d_{xy} shifts closer to $\mathcal{E}_{\mathcal{F}}$ and takes over the role of magnetic orbital. The reversal of the roles is a consequence of the change of symmetry and reduced coordination, which alters hybridization amplitudes (see hybridization Table V) and consequently modifies the widths and effective orbital splittings of 3d levels.

To understand the energetics of Co adsorption on graphene nanoribbons we performed a series of calculations for different vertical distances of Co and nanoribbon plane. The calculated equilibrium heights of the adatom together with adsorption energies are summarized in Table II. The formed covalent bonds are directional and the bond strength depends on the adatom coordination. Therefore it is unsurprising that the adsorption energy is strongly dependent on the adsorption site. The presented energies are the minimal values obtained after relaxation. A comparison of total energy curves for different positions of impurity and a comment on the role of correlations in adsorption energy are given in Appendix A.

Table III presents GGA-PBE orbital occupations and total and orbital contributions to magnetic moments of Co for the h_0, h_1, and h_2 positions, which correspond to the earlier presented local densities of states (Fig. 5). Magnetic moments of Co at the ZGNR depend on the adsorption site, but their absolute values in all cases are much smaller than the moment of the free atom ($\mathcal{M}_{\mathrm{Co}} \approx 3\ \mu_B$ [47]). The decrease of magnetic moment is dictated by electron transfer from 4s to 3d states and corresponding change of occupancy of the unpaired 3d orbitals. The spin-down component of the hybrid states is almost entirely below $\mathcal{E}_{\mathcal{F}}$, while a large portion of the spin-up component lies above $\mathcal{E}_{\mathcal{F}}$. As aforementioned, in the case of hollow sites of ZGNRs magnetic moments come mainly from d_{xz} and d_{yz} orbitals and their contributions are 1.103 and 0.941 for h_1 and h_2, respectively; i.e., they do not differ much from unity. We have checked that the trend of decrease of moment with moving with the adsorption site to the center of the ribbon persists in wider ribbons and for $N = 12$ total magnetic moment reaches at the center $\mathcal{M} = 1.091$, which is close to the value for the Co adatom on graphene ($\mathcal{M} = 1.083$), as shown in Table IV. Similarly binding energy in the center of a wide ribbon converges to the value for graphene $\mathcal{E}_{\mathrm{ads}} = -1.2$ eV; for $N = 12$ amounts value $\mathcal{E}^{h_6}_{\mathrm{ads}} = -1.23$ eV.

Figures 6(a) and 6(b) show LDA spin polarization patterns induced by the presence of the Co adatom at the h_1 and h_2 sites calculated for the 8 × 1 supercell. For the twice reduced supercell (4 × 1) the local polarizations around the impurity are almost identical to the 8 × 1 case; the differences are only seen at the border of the supercells. In the case of the 4 × 1 cell the edge magnetic moments at a greater distance from the impurity do not approach the values for the pure nanoribbon; this is achieved for the 8 × 1 cell. As is seen from Fig. 6 the polarization effect is strongest for Co located in the h_1 position and the nearest edge atoms are most sensitive to perturbation. Our calculations indicate the charge transfer from Co to the π bands of nanoribbon and no transfer is observed to the σ bands. The occupation of the neighboring carbon p_z orbitals is increased with adsorption and the spin polarization of the nearby atoms at the edge is locally suppressed.

III. KONDO EFFECT OF Co ATOM ON HOLLOW SITE

A. Model

Static mean field DFT description of the electronic structure of Co adsorbed on the nanoribbon does not capture the effects of dynamic correlations of strongly interacting 3d electrons. To complement the missing local correlations of adatom electrons we complete the model by a Hubbard-type term and exchange [83,84]. The description of the nanoribbon substrate and its coupling to the impurity is maintained within DFT formalism. The Kohn-Sham Hamiltonian thereby serves as the noninteracting reference frame onto which we add local intra-atomic interactions. As we have presented in the preceding section, in the case of the considered hollow location of the Co atom the d_{xz} and d_{yz} orbitals are responsible for formation of magnetic moment; their fluctuations in occupations and spins are essential for low-energy physics. We discuss therefore the double-orbital Anderson-like Hamiltonian in the form

$$\mathcal{H} = \mathcal{H}_d + \mathcal{H}_v + \mathcal{H}_{\mathrm{ZGNR}}, \tag{2}$$

where the impurity is described by

$$\mathcal{H}_d = \sum_{m\sigma} \varepsilon_0 n_{m\sigma} + \mathcal{U} \sum_m n_{m+} n_{m-} + (\mathcal{U} - \mathcal{J}/2) n_m n_{m'} - 2\mathcal{J} \vec{\mathcal{S}}_m \cdot \vec{\mathcal{S}}_{m'}, \tag{3}$$

where $m = xz(yz)$ and ε_0 is the bare energy of local levels, assumed to be equal for both orbitals; $\mathcal{U}$ is the energy of intra- or interorbital Coulomb interaction and $\mathcal{J}$ is Hund's exchange coupling. The nanoribbon Hamiltonian reads

$$\mathcal{H}_{\mathrm{ZGNR}} = \sum_{kn\sigma} \epsilon_{kn\sigma} c^{\dagger}_{kn\sigma} c_{kn\sigma}, \tag{4}$$

with $\varepsilon_{kn\sigma}$ denoting DFT ribbon eigenvalues and corresponding eigenfunctions $|kn\sigma\rangle$. The interaction between nanoribbon electrons and local levels is described by the hybridization term

$$\mathcal{H}_v = \sum_{kn\sigma m} (\mathcal{V}_{kn\sigma m} c^{\dagger}_{kn\sigma} d_{m\sigma} + \mathrm{H.c.}), \tag{5}$$

TABLE III. Magnetic moments and spin occupancies of different Co d orbitals for hollow positions of 4ZGNR (VASP).

	h_0			h_1			h_2		
d	$\mathcal{N}_+$	$\mathcal{N}_-$	$\mathcal{M}$	$\mathcal{N}_+$	$\mathcal{N}_-$	$\mathcal{M}$	$\mathcal{N}_+$	$\mathcal{N}_-$	$\mathcal{M}$
z^2	0.966	0.933	0.033	0.997	0.994	0.003	0.996	0.989	0.007
xz	0.963	0.456	0.507	0.963	0.503	0.46	0.937	0.729	0.208
yz	0.955	0.889	0.066	0.979	0.336	0.643	0.978	0.245	0.733
xy	0.997	0.062	0.935	0.934	0.837	0.097	0.905	0.845	0.06
x^2-y^2	0.965	0.926	0.039	0.892	0.763	0.129	0.879	0.782	0.097
tot (d)			1.579			1.332			1.105

where hybridization amplitudes $V_{kn\sigma m}$ are hopping matrix elements between nanoribbon DFT eigenstates and d orbitals. In this work, the realistic *ab initio* hybridization is taken from GGA-PBE calculations based on the VASP code. Hybridization strengths we use are not strictly single-impurity couplings due to the periodicity of the adopted first-principles computations schemes, but for large enough supercells they can approximately play this role. The nearest-neighbor impurity-nanoribbon hopping integrals are extracted from DFT data $V_m^i = \sum_{kn} \langle d_m|\overline{kn}\rangle \overline{\varepsilon_{kn}} \langle \overline{kn}|p_z^i\rangle$, where $|m\rangle$ denotes adatom orbital, $|\overline{kn}\rangle$ and $\overline{\varepsilon_{kn}}$ are DFT eigenstates and energies of the Co+ZGNR system, and the sum runs over Kohn-Sham eigenstates in the energy range $|\mathcal{E}| < 6$ eV. Table V presents hybridization amplitudes in real space with restriction to the dominant n.n. contributions. For comparison we present amplitudes for all 3d orbitals. Note the smallness of the amplitudes to A_1 and B_2 for d_{xz} in the h_1 position and large amplitudes to these atoms for d_{yz}. Pictorially this difference can be understood recalling the shapes of these orbitals. Remembering that the edge states dominate the energy window near the gap, one can expect distinctly different roles of d_{xz} and d_{yz} orbitals in Kondo physics for the h_1 position. For h_2 the role of edge states is diminished. Comparison of the amplitudes for h_0 and hollow sites helps to understand the earlier mentioned reversal of the roles between d_{yz} and d_{xy} when positions of the adatom interchange.

To describe orbital degrees of freedom on the same footing as spin it is useful to introduce orbital pseudospin $\mathcal{T}$ defined by $\mathcal{T} = \Psi_d^\dagger \tau \Psi_d$, where τ is the Pauli matrix in orbital space $\{d_{xz},d_{yz}\}$ and $\Psi_d^\dagger$ represents the spin-orbital field operator $\Psi_d^\dagger = [d_{xz+}^\dagger,d_{xz-}^\dagger,d_{yz+}^\dagger,d_{yz-}^\dagger]$.

B. Hybridization function

The hybridization function describes coupling of impurity to nanoribbon. Hereafter we restrict ourselves to nearest neighbors of the impurity and consider only d_{xz} and d_{yz} orbitals. The hybridization then reads

$$\Sigma_{mm'\sigma}^{h_{1(2)}} = \sum_{kn} \frac{V_{kn\sigma m}^{*h_{1(2)}} V_{kn\sigma m'}^{h_{1(2)}}}{z - \varepsilon_{kn\sigma}}, \tag{6}$$

where $\varepsilon_{kn\sigma}$ and $|kn\sigma\rangle$ are DFT eigenenergies and eigenstates of bare graphene nanoribbon and $V_{kn\sigma m} = (1/\sqrt{N_x}) \sum_{l_h} \sum_{a_h} V_m^{a_h} e^{ika_h} \langle kl_h\sigma|kn\sigma\rangle$, where a_h are n.n. vectors connecting the adatom with carbon sites from the surrounding hexagon, l_h labels four carbon chains along the infinite x direction crossing the hexagon, N_x is the number of sites in the carbon chain in the x direction, and $|kl\rangle = (1/\sqrt{N_x}) \sum e^{iki_l} |p_z^{i_l}\rangle$. All hybridization functions presented below have been calculated using the VASP code. For pure graphene $\Sigma_{mm'} \sim \delta_{mm'}$ due to C_{6v} symmetry of hollow sites. In nanoribbons, where this symmetry is broken, also off-diagonal terms occur, but as we have checked due to rapid oscillations in k space they are much smaller than diagonal elements and additionally they affect the impurity states in fourth power in hybridization, whereas the diagonal in second power. Based on

TABLE IV. Total magnetic moments of Co atoms located in hollow positions of NZGNR ($N = 4,6,8$) compared with magnetic moment of Co at hollow site of graphene ($\mathcal{G}$) (VASP with GGA-PBE).

	$\mathcal{M}$	$\mathcal{M}_{h_1}$	$\mathcal{M}_{h_2}$	$\mathcal{M}_{h_3}$	$\mathcal{M}_{h_4}$
$\mathcal{G}$ + Co	1.083				
4ZGNR + Co		1.413	1.178		
6ZGNR + Co		1.383	1.209	1.122	
8ZGNR + Co		1.376	1.258	1.180	1.115

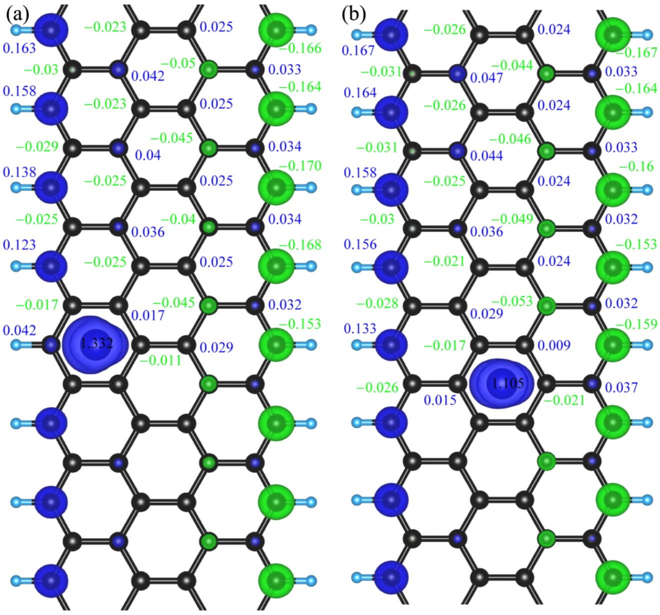

FIG. 6. (Color online) Spin density plots of Co adatom and 4ZGNR matrix (8×1 supercell). The blue/dark gray densities correspond to spin-up and green/light gray to spin-down components. (a) Co impurity in h_1 position. (b) Co in h_2 position.

TABLE V. Nearest-neighbor hybridization amplitudes (in eV) of Co adatom located in hollow positions of 4ZGNR.

	h_0		h_1				h_2			
d	$\lvert\mathcal{V}_d^{\mathcal{A}_1}\rvert$	$\lvert\mathcal{V}_d^{\mathcal{B}_1}\rvert$	$\lvert\mathcal{V}_d^{\mathcal{A}_1}\rvert$	$\lvert\mathcal{V}_d^{\mathcal{A}_2}\rvert$	$\lvert\mathcal{V}_d^{\mathcal{B}_1}\rvert$	$\lvert\mathcal{V}_d^{\mathcal{B}_2}\rvert$	$\lvert\mathcal{V}_d^{\mathcal{A}_2}\rvert$	$\lvert\mathcal{V}_d^{\mathcal{A}_3}\rvert$	$\lvert\mathcal{V}_d^{\mathcal{B}_2}\rvert$	$\lvert\mathcal{V}_d^{\mathcal{B}_3}\rvert$
z^2	0.13	0.64	0.01	0.01	0.01	0.01	0.01	0.01	0.01	0.01
xz	0.47	0	0.01	0.48	0.47	0.01	0.01	0.48	0.47	0.01
yz	0.13	0.65	0.92	0.28	0.28	0.9	0.89	0.27	0.27	0.89
xy	0.47	0	0.03	0.31	0.31	0.02	0.02	0.31	0.31	0.02
x^2-y^2	0.3	0.52	0.59	0.19	0.16	0.57	0.58	0.18	0.18	0.58

these arguments we neglect in the following, for simplicity of calculations, the off-diagonal self-energies. The hybridization function plays the role of embedding self-energy. The real parts of self-energies are associated with the shift of the local energies, while the imaginary parts give the broadening of impurity levels. Figure 7 shows the imaginary part of the low-energy hybridization functions for the h_1 position together with the corresponding VASP nanoribbon bands from this range. In the following we refer to the presented singularities and therefore we introduce their labeling in Fig. 7(b). More detailed pictures of spin- and orbital-resolved hybridization with both real and imaginary parts are presented in Fig. 8. In general the hybridization functions are spin dependent, which is mainly dictated by spin dependence of local nanoribbon Green's functions. The opposite local polarizations at h_1 and h_3 (Fig. 1) are reflected in the change of roles of spins in hybridization function $\Sigma^{h_1}_{m\sigma} = \Sigma^{h_3}_{m\bar{\sigma}}$. At h_2 (Fig. 9), where polarization contributions from the opposite edges compensate, hybridizations are equal for both spin orientations. The hybridization functions are rich in structure; of special importance for the Kondo effect are observed Van Hove singularities (VHSs) occurring in position of minima, maxima, or saddle points of the bands. Vanishing of derivatives of dispersion curves indicates energies where singularities are expected, but whether the singularity is clearly reflected in orbital-resolved hybridization depends on the weight of the contribution of a given symmetry to the bands in the considered energy range. This fact is illustrated in Figs. 7(c) and 7(d), where highest conduction and lowest valence bands are decorated by amplitudes specifying projection of the eigenfunctions onto the symmetry of a given local orbital. For example in the energy window presented in Figs. 7(c) and 7(d) two pronounced singularities are observed (VH1ν and VH2ν) below the gap for yz symmetry, characterized by peaks in imaginary parts of hybridizations and discontinuities in real

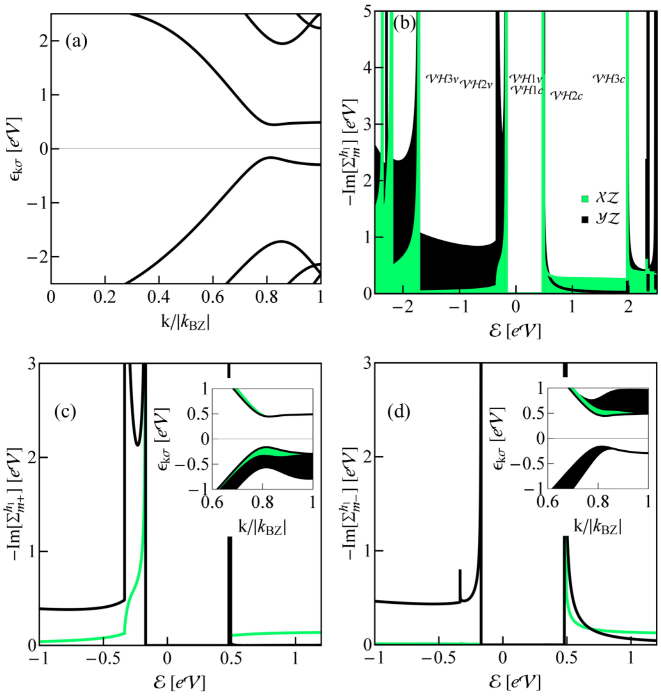

FIG. 7. (Color online) Low-energy band structure of 4ZGNR (a) together with orbitally resolved hybridization functions of Co adatom in h_1 position [(b), (c), (d)]. Black color denotes yz contribution and green/light gray xz. In (b) labeling of Van Hove singularities used further in the text is introduced. Panels (c) and (d) present spin-up and spin-down parts of hybridization, respectively. Insets of (c) and (d) are zoom views of lowest dispersion curves decorated with xz and yz contributions.

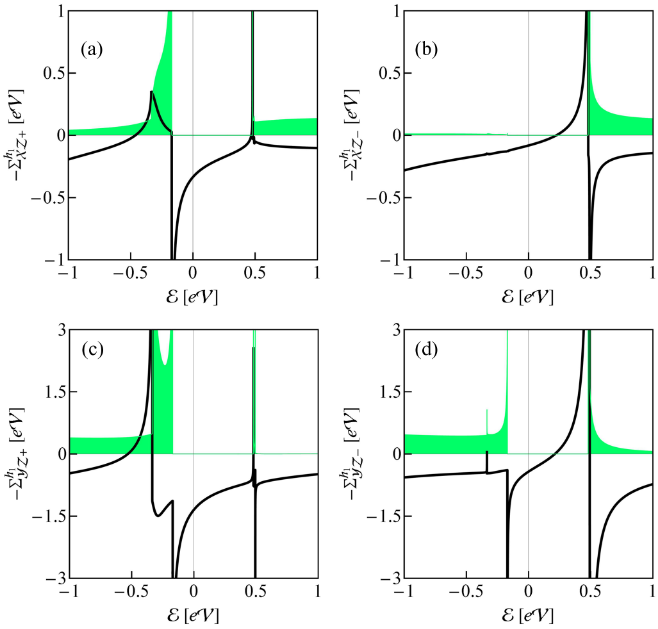

FIG. 8. (Color online) Orbital- and spin-resolved hybridization functions for Co at h_1 position in 4ZGNR. Solid black lines represent real parts (Re[$\Sigma^{h_1}_{m\sigma}$]) and imaginary parts (Im[$\Sigma^{h_1}_{m\sigma}$]) are shown by green/light gray filled curves.

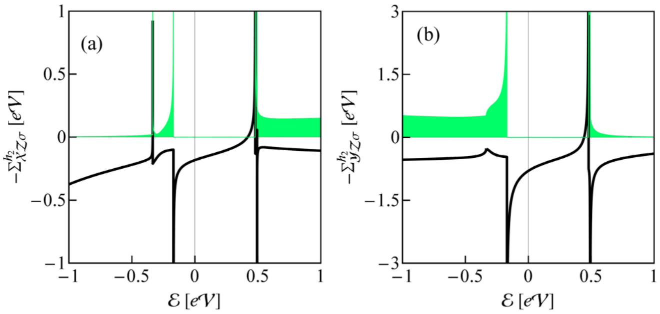

FIG. 9. (Color online) Orbital-resolved hybridization function of Co in h_2 position of 4ZGNR. Solid black lines represent real part and green/light gray filled curves show the imaginary parts of hybridization.

parts. For xz symmetry on the other hand, similar behavior is seen only close to the gap. For $\mathcal{E} = -0.3348$ eV (VH2ν) the xz contribution to the bands is small [see the insets of Figs. 7(c) and 7(d)]. The character of many-body resonances is determined by the deepness of the local level with respect to the Fermi energy and hybridization strength; both of these values dramatically change near the singularity and therefore it is expected that an interesting physics emerges in the vicinity of these energy points.

C. Slave boson mean field approach

The described modeling of a single adatom embedded onto a graphene nanoribbon by the Anderson-like Hamiltonian allows us to examine the strong correlations by the well elaborated techniques with known applicability regimes. Our main interest focuses on the impact of the details of the nanoribbon electronic and magnetic structure on the single-impurity Kondo effect. The basic analysis of variation of many-body correlations with tuning the chemical potential is based on the mean field slave boson approach of Kotliar and Ruckenstein [49]. This approximation concentrates exclusively on many-body resonances taking into account spin and orbital fluctuations, but neglecting charge fluctuations. In principle SBMFA strictly applies close to the unitary Kondo limit, but due to its simplicity this method is also often used for systems with broken symmetry [85–88]. It is believed that it captures the essential features of the examined problem also in this case. SBMFA is unreliable for higher temperatures. This is a consequence of a break of the required gauge invariance which is associated with charge conservation, what leads to an artificial sharp transition to the state with vanishing expectation value of boson fields [48]. To get some insight into the higher temperatures regime and to see the influence of charge fluctuations we complement the analysis in the next section by presentation of some NCA results (fluctuation of boson fields) and EOM calculations. For brevity the discussion of the latter results is restricted only to a single value of chemical potential.

In Kotliar and Ruckenstein (KR) formalism one introduces a set of boson operators for each electronic configuration of the impurity. For the considered two-orbital impurity there are 16 auxiliary Bose fields projecting onto the empty (e), single occupied ($p_{m\sigma}$), doubly occupied (d_ν, with $\nu = \mathcal{S}\mathcal{S}_z$ or $\nu = \mathcal{T}\mathcal{T}_z$, i.e., $\nu = \mathcal{S}1,\mathcal{S}0,\mathcal{S}\bar{1},\mathcal{T}1,\mathcal{T}0,\mathcal{T}\bar{1}$), triple occupied ($t_{m\sigma}$), and fully (quadruple) occupied (f) states [50]. For e and p operators the assignment of eigenstates is clear, for the t operator we use the notation $t_{m\sigma} \leftrightarrow |m\sigma,\overline{m}\uparrow\overline{m}\downarrow\rangle$, and the eigenstates corresponding to d_ν are listed in Table VI. In order to eliminate unphysical states the completeness relation for these operators $\mathcal{I} = e^\dagger e + \sum_{m\sigma} p^\dagger_{m\sigma} p_{m\sigma} + \sum_\nu d^\dagger_\nu d_\nu + \sum_{m\sigma} t^\dagger_{m\sigma} t_{m\sigma} + f^\dagger f$, and the correspondence between fermions and bosons $[\mathcal{Q}_{m\sigma} = p^\dagger_{m\sigma} p_{m\sigma} + d^\dagger_{\mathcal{S}\mathcal{S}_z(\sigma)} d_{\mathcal{S}\mathcal{S}_z(\sigma)} + (\frac{1}{2})(d^\dagger_{\mathcal{S}0} d_{\mathcal{S}0} + d^\dagger_{\mathcal{T}0} d_{\mathcal{T}0}) + d^\dagger_{\mathcal{T}\mathcal{T}_z(m)} d_{\mathcal{T}\mathcal{T}_z(m)} + t^\dagger_{m\sigma} t_{m\sigma} + \sum_{\sigma'} t^\dagger_{\overline{m}\sigma'} t_{\overline{m}\sigma'}]$ has to be imposed $[\mathcal{S}_z(\pm) = 1(\bar{1})$ and $\mathcal{T}_z[xz(yz)] = 1(\bar{1})]$. These constraints can be enforced by introducing Lagrange multipliers $\lambda,\lambda_{m\sigma}$ and the effective SB Hamiltonian then reads

TABLE VI. Two electron eigenstates of Hamiltonian (3) with the assigned slave bosons.

Eigenstate	Slave boson
$\lvert\uparrow,\uparrow\rangle$	$d_{\mathcal{S}=1\mathcal{S}_z=1} = d_{\mathcal{S}1}$
$(1/\sqrt{2})(\lvert\uparrow,\downarrow\rangle + \lvert\downarrow,\uparrow\rangle)$	$d_{\mathcal{S}=1\mathcal{S}_z=0} = d_{\mathcal{S}0}$
$\lvert\downarrow,\downarrow\rangle$	$d_{\mathcal{S}=1\mathcal{S}_z=\bar{1}} = d_{\mathcal{S}\bar{1}}$
$\lvert\uparrow\downarrow,0\rangle$	$d_{\mathcal{T}=1\mathcal{T}_z=1} = d_{\mathcal{T}1}$
$(1/\sqrt{2})(\lvert\uparrow,\downarrow\rangle - \lvert\downarrow,\uparrow\rangle)$	$d_{\mathcal{T}=1\mathcal{T}_z=0} = d_{\mathcal{T}0}$
$\lvert 0,\uparrow\downarrow\rangle$	$d_{\mathcal{T}=1\mathcal{T}_z=\bar{1}} = d_{\mathcal{T}\bar{1}}$

$$
\begin{aligned}
\mathcal{H}^{\mathcal{K}-\mathcal{R}} = & \sum_{m\sigma} (\mathcal{E}_0 + \lambda_{m\sigma}) n^f_{m\sigma} + \lambda(\mathcal{I} - 1) \\
& + \sum_{m\sigma} \lambda_{m\sigma} \left(\mathcal{Q}_{m\sigma} - n^f_{m\sigma}\right) + (\mathcal{U} - \mathcal{J}) \sum_{\mathcal{S}_z} d^\dagger_{\mathcal{S}\mathcal{S}_z} d_{\mathcal{S}\mathcal{S}_z} \\
& + \sum_{\mathcal{T}_z} [\mathcal{U} + (1 - |\mathcal{T}_z|)\mathcal{J}] d^\dagger_{\mathcal{T}\mathcal{T}_z} d_{\mathcal{T}\mathcal{T}_z} \\
& + (3\mathcal{U} - \mathcal{J}) \sum_{m\sigma} t^\dagger_{m\sigma} t_{m\sigma} + (6\mathcal{U} - 2\mathcal{J}) f^\dagger f \\
& + \sum_{kn\sigma m} \left(\mathcal{V}^{h_{1(2)}}_{kn\sigma m} c^\dagger_{kn\sigma} z_{m\sigma} f_{m\sigma} + \text{H.c.}\right) + \mathcal{H}_{\text{ZGNR}}.
\end{aligned} \tag{7}
$$

The effective hopping in Eq. (7) is expressed by $z^+_{m\sigma} f^+_{m\sigma}$ ($z_{m\sigma} f_{m\sigma}$) with $z_{m\sigma} = [e^+ p_{m\sigma} + p^+_{m\overline{\sigma}} d_{\mathcal{S}\mathcal{S}_z(\sigma)} + p^+_{\overline{m\sigma}}(\frac{1}{2})(d_{\mathcal{S}0} + d_{\mathcal{T}0}) + p^+_{\overline{m}\sigma} d_{\mathcal{T}\mathcal{T}_z(m)} + d^+_{\mathcal{T}\overline{\mathcal{T}_z(m)}} t_{m\sigma} + (\frac{1}{2})(d^+_{\mathcal{S}0} + d^+_{\mathcal{T}0}) t_{\overline{m}\sigma} + d^+_{\overline{\mathcal{S}\mathcal{S}_z(\sigma)}} t_{\overline{m\sigma}} + t^+_{m\overline{\sigma}} f]/(\sqrt{\mathcal{Q}_{m\sigma}}\sqrt{1 - \mathcal{Q}_{m\sigma}})$.

The stable mean field solutions are found from the saddle point of the partition function of (7), i.e., from the minimum of the free energy with respect to the slave boson parameters and Lagrange multipliers. The results for the h_1 and h_2 positions are presented in Figs. 10–15. According to our earlier DFT discussion we restrict ourselves to the two-orbital subspace (d_{xz}, d_{yz}) considering the case of triple electron occupancy (single hole) and choosing a typical for Co on graphene nanostructure Coulomb interaction parameter $\mathcal{U} = 3$ eV [46,47,89] and the bare orbital level energy $\mathcal{E}_0 = -(2\mathcal{U} + \mathcal{U})/2 = -7.5$ eV. This choice of parameters yields within the Hartree-Fock approximation the required

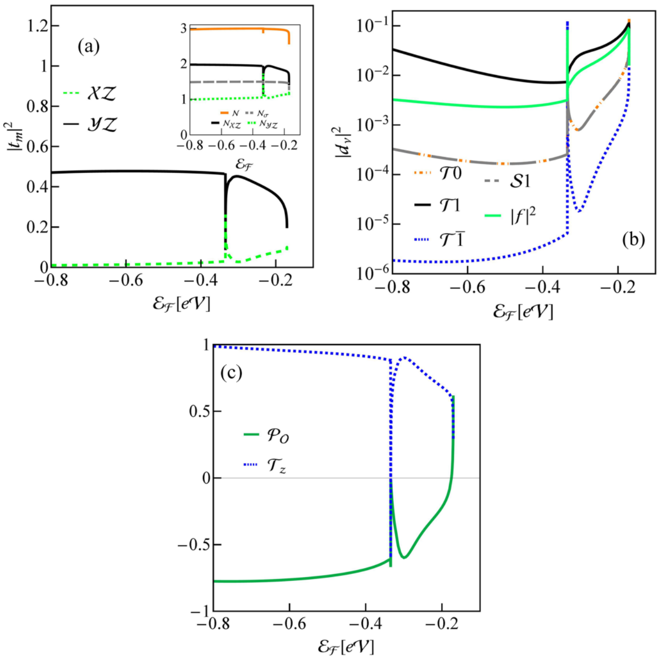

FIG. 10. (Color online) Expectation values of slave boson operators, polarizations, and expectation values of orbital pseudospin of Co impurity at h_2 position of 4ZGNR: (a) triple occupation slave boson operators $|t_m|^2 = |t_{m+}|^2 = |t_{m-}|^2$; (b) double and full occupation slave boson operators $|d_{\mathcal{T}0}|^2$, $|d_{\mathcal{T}1}|^2$, $|d_{\mathcal{T}\bar{1}}|^2$, $|d_{\mathcal{S}1}|^2 = |d_{\mathcal{S}\bar{1}}|^2$, $|d_{\mathcal{S}0}|^2 = |d_{\mathcal{T}0}|^2$, and $|f|^2$; (c) orbital polarization of Co at h_2 site [$\mathcal{P}_\mathcal{O} = \frac{\varrho_{xz}(\mathcal{E_F})-\varrho_{yz}(\mathcal{E_F})}{\varrho_{xz}(\mathcal{E_F})+\varrho_{yz}(\mathcal{E_F})}$, where $\varrho_m(\mathcal{E}) = \sum_\sigma \varrho_{m\sigma}(\mathcal{E})$ and $\varrho_{m\sigma}$ denotes spin-orbital partial density of states] and expectation value of Co orbital pseudospin ($\mathcal{T}_z$). Inset of (a) shows total, spin, and orbital d_{xz},d_{yz} occupancies.

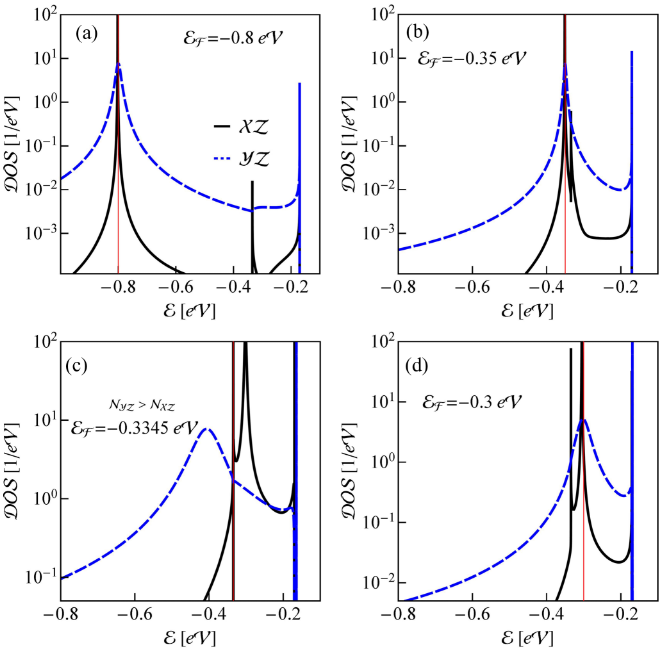

FIG. 11. (Color online) Selected partial orbital DOS of Co at h_2 site in 4ZGNR. The vertical red/thin lines indicate positions of Fermi levels.

triple occupancy ($\mathcal{N} = 3$) and reproduces the DFT magnetic moments.

Let us first discuss the h_2 case, where the local nanoribbon environment is unpolarized. Figure 10 presents expectation values of slave boson operators, orbital and spin occupations, orbital pseudospin, and orbital polarization, all quantities plotted as a function of chemical potential. To interpret the results it is worth referring to the energy dependence of the corresponding hybridization functions (Fig. 9). Outside the singularities ($-0.8 < \mathcal{E} < -0.4$), where the hybridization function of yz symmetry dominates over xz hybridization, Kondo physics is governed mainly by spin fluctuations in the yz sector ($\mathcal{N}_{yz} \approx 1$); orbital xz is almost completely filled ($\mathcal{N}_{xz} \approx 2$). We have checked that there are no SBMFA solutions for the xz channel when the interorbital fluctuation path is closed [i.e., when the two last terms in (3) are neglected]. When the interorbital path opens the coupled spin-orbital fluctuations create resonances in both orbital sectors. Very crudely one can visualize these processes as virtual complete filling or emptying of yz orbital by hoppings resulting in fast SU(2) type spin fluctuations in the yz channel (broad peak). These fluctuations are however not completely decoupled from the xz channel. Orbital xz is much weaker coupled to nanoribbon and hoppings are less frequent. Virtual creation of a hole on the xz orbital increases the probability of double occupancy of the yz orbital. Temporary reverse of roles of orbitals is possible. Such orbital fluctuations enable weak effective spin fluctuations in the xz sector despite its high occupancy. The average time of such fluctuations is however relatively long, which is reflected in an observed narrow xz quasiparticle resonance. The representative density of states of the h_2 impurity in this range ($\mathcal{E_F} = -0.8$ eV) is shown in Fig. 11. When $\mathcal{E_F}$ moves closer to singularity VH2ν, yz hybridization does not change considerably, but in the xz sector the Van Hove singularity manifests strongly. Close to VH2ν the expectation values of slave boson operators t and orbital occupations for both symmetries approach each other in consequence of strong enhancement of xz hybridization, but the symmetric SU(4) case is not realized for any energy because this would require the equality of both real and imaginary parts of hybridizations functions. As seen in Fig. 11(b), the resonances in this region for both orbitals ($\mathcal{E} = -0.35$ eV) are distinctively different. Interestingly, moving still closer to the singularity around $\mathcal{E} = -0.3345$ eV, in an extremely narrow energy range, orbital xz even takes over the dominant role in many-body processes, which is reflected in a change of sign of orbital pseudospin. In the region of singularity strong deviations of orbital occupancies from integer values are observed which indicates that the system is driven out from the Kondo state into a mixed valence state. For the chemical potential above VH2ν again the dominance of the yz orbital is restored and the system moves into the Kondo state again. One should remember however that the presented picture in the vicinity of the singularity should be treated with caution, only as a crude visualization of tendencies. Around the singularity the system is pushed into the non-Fermi liquid regime due to the observed divergences of self-energies, and in principle for a discussion of this range summation of higher order corrections

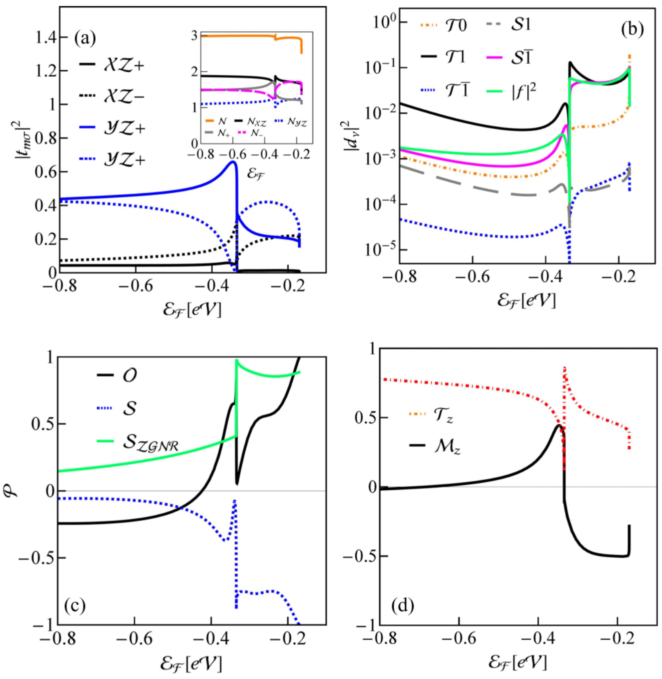

FIG. 12. (Color online) Expectation values of slave boson operators, polarizations, and expectation values of orbital pseudospin and magnetic moment of Co impurity at h_1 position of 4ZGNR: (a) triple-occupation slave boson operators $|t_{m\sigma}|^2$; (b) double- and full-occupation SB operators $|d_{\mathcal{T}0}|^2$, $|d_{\mathcal{T}1}|^2$, $|d_{\mathcal{T}\bar{1}}|^2$, $|d_{\mathcal{S}1}|^2$, $|d_{\mathcal{S}\bar{1}}|^2$, $|d_{\mathcal{S}0}|^2 = |d_{\mathcal{T}0}|^2$, and $|f|^2$; (c) local spin polarization of the nanoribbon around h_1 ($\mathcal{P}_{\mathcal{S}_{\text{ZGNR}}} = \sum_i \frac{\varrho_{i+}(\mathcal{E}_\mathcal{F})-\varrho_{i-}(\mathcal{E}_\mathcal{F})}{\varrho_{i+}(\mathcal{E}_\mathcal{F})+\varrho_{i-}(\mathcal{E}_\mathcal{F})}$, where $\varrho_{i\sigma}$ denotes local ZGNR density of states at the n.n. carbon sites around hollow position), orbital ($\mathcal{P}_\mathcal{O}$) and spin polarization of Co adatom ($\mathcal{P}_\mathcal{S}$); (d) magnetic moment and orbital pseudospin of Co impurity. Inset of (a) presents spin- and orbital-resolved contributions to the occupancies of Co.

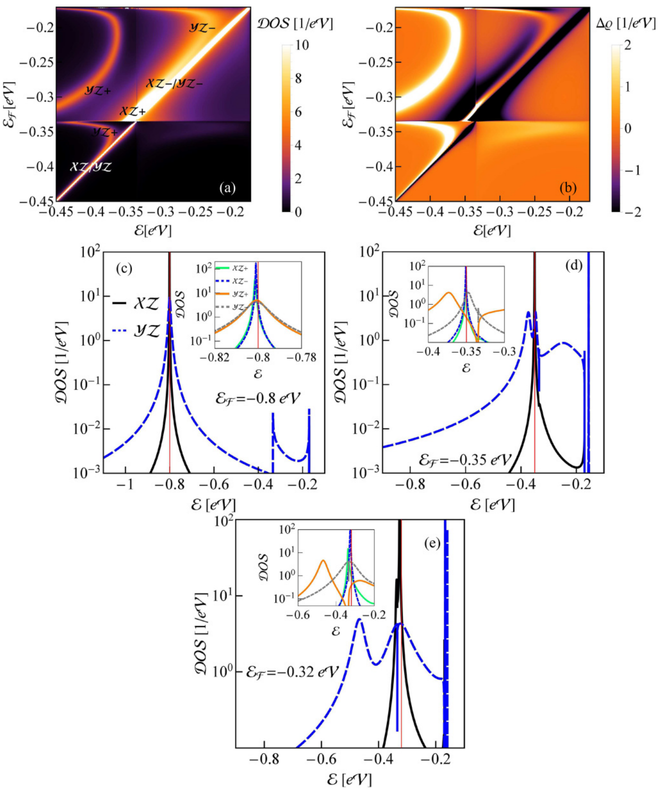

FIG. 13. (Color online) (a) Density of states map of Co impurity in h_1 position of 4ZGNR. (b) $\Delta\varrho$, difference of spin-up and spin-down densities of states of Co at h_1 site of 4ZGNR. (c), (d), (e) Partial orbital densities of states for the selected values of the Fermi levels. Insets are the zoom views of the spin- and orbital-resolved DOS.

to MFA is indispensable [90,91]. When $\mathcal{E}_\mathcal{F}$ moves closer to the edge and both real and imaginary parts of hybridization are strongly enhanced for both symmetries, broadening of many-body resonances results and delta-like structures are observed at the band edges, which extend into the gap for $\mathcal{E}_\mathcal{F}$ moving very close to the edge [Figs. 11(c) and 11(d)]. They reflect the new poles of the impurity Green's function and these structures are essential in order to satisfy the sum rules. Of interest are also the dips occurring for energies where singularities occur. They emerge due to an interplay of correlations effect and singular substrate electron density of states. When the Fermi level crosses the singularity the dip sits at the the Fermi level, but singularities are also reflected in the spectral function when the chemical potential is not in close proximity to the VHS (Fig. 11).

Let us now turn to the h_1 case. The spin polarization of nanoribbon breaks the spin degeneracy. The number of independent slave boson operators increases (Fig. 12) and the many-body resonances become spin dependent (Fig. 13). Again of special interest are the regions around singularities of DOS. In addition to the earlier described effects, also new phenomena associated with polarization are observed. The sharp change of local nanoribbon spin polarization in the vicinity of VH2ν is revealed in a drastic but opposite change of impurity polarization and suppression of screening processes of Co magnetic moment. The singularity is most strongly reflected in the abrupt increase of spin distinction in the yz orbital channel which is a consequence of clearly exhibited singularity in the corresponding hybridization function for one spin direction and only a very weak trace of it for the opposite spin. Remarkable is the resulting jump and change of sign of magnetic moment and the fall and next jump of orbital pseudospin when $\mathcal{E}_\mathcal{F}$ crosses the singularity. All the anomalies are the consequence of the dramatically enhanced imaginary part of hybridization and a jump from negative to positive values of the real part of hybridization. The dramatic changes of spin or orbital characteristics when the Fermi level crosses the singularities are of potential interest for spintronics (orbitronics), because these changes can be induced by gate voltage.

Figure 13(a) illustrates the evolution of density of states with the shift of the Fermi level. The clearly seen horizontal ($\mathcal{E}_\mathcal{F} = -0.3348$ eV) and vertical ($\mathcal{E} = -0.3348$ eV) straight lines of reduced intensity reflect the position of VH2ν singularity. In principle STM spectroscopy, which is used to probe local densities of states, is capably read off the information encoded in this map, assuming that a suitable treatment of interference effects of different paths will be performed. We shortly comment on this point in our conclusions. To highlight the origin of the peaks of density of states (high-intensity lines),

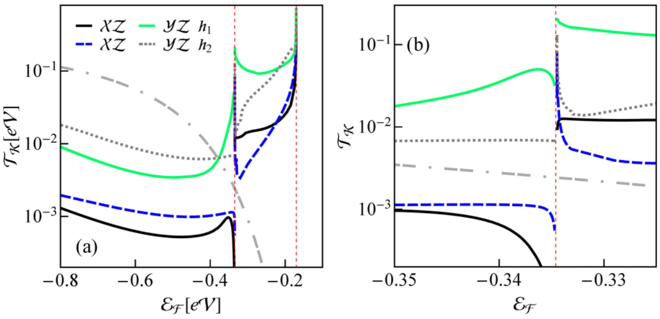

FIG. 14. (Color online) Characteristic quasiparticle temperatures T_K of Co in 4ZGNR for xz and yz channels vs position of the Fermi level. Dash-dotted line represents Kondo temperature of Co at hollow position in graphene. Panel (b) shows details of dependencies close to VH2ν singularity.

we have put on the map information on the spin-orbital contributions. Figure 13(b) shows the difference of densities of states for spin up and spin down; this quantity should be detectable by the spin-polarized STM technique [92]. The representative spin- and orbital-resolved densities of states, which correspond to the selected horizontal cross sections ($\mathcal{E}_F = \text{const.}$) of the map [Fig. 13(a)] are displayed in Figs. 13(c)–13(e). Since in the considered energy range yz hybridization is stronger than for xz symmetry the corresponding many-body yz resonances are in general broader. Although spin distinction in the xz hybridization is remarkable (Fig. 8) it is not reflected in clear distinction of corresponding many-body peaks (Fig. 13). This observation is in accordance with our earlier interpretation of the xz resonance as a repercussion of spin fluctuations in the yz shell transferred to xz by orbital fluctuations. In contrast to the h_2 case, for the h_1 position the VH2ν singularity plays an important role for yz symmetry, especially for majority spins. The peak splitting of the yz resonance is a combined effect of spin dependence and singularity-induced dips in the corresponding densities of states. Figure 14 presents Kondo temperatures for the h_1 and h_2 positions. We define T_K through widths and position of quasiparticle resonance [48]. $T_{Km} = (1/2)\sum_\sigma \sqrt{\widetilde{\Delta}^2_{m\sigma} + \widetilde{\mathcal{E}}^2_{m\sigma}}$, where $\widetilde{\mathcal{E}}_{m\sigma}$ is the distance between Fermi energy and quasiparticle resonance and $\widetilde{\Delta}_{m\sigma}$ is the width at half maximum. Since the characteristic quasiparticle energies are distinctively different for both orbital channels we show the corresponding characteristic temperatures separately. The estimated characteristic temperatures are of the order of 20 K and 200 K for the xz and yz channels, respectively, and they are strongly enhanced or suppressed in the region of the singularity depending on which side the chemical potential approaches the singularity. This tendency reflects the opposite shift of effective orbital energies on both sides caused by real parts of self-energy, which are discontinuous and change sign in the singularity point. For comparison we also plot in Fig. 14 the gate voltage dependence of the Kondo temperature for pure graphene. In accordance with earlier reports [46] and discussion on the requirement of critical hybridization for the occurrence of the Kondo effect in gapless systems [93], the Kondo effect is not observed for the undoped graphene. Around $\mathcal{E}_F = -0.2$ eV, T_K takes a value of 0.1 K; for $\mathcal{E}_F = -0.3$ eV, T_K reaches 10 K; and since graphene Van Hove singularities are far away outside the examined energy range, the Kondo temperature monotonically increases with lowering of the chemical potential.

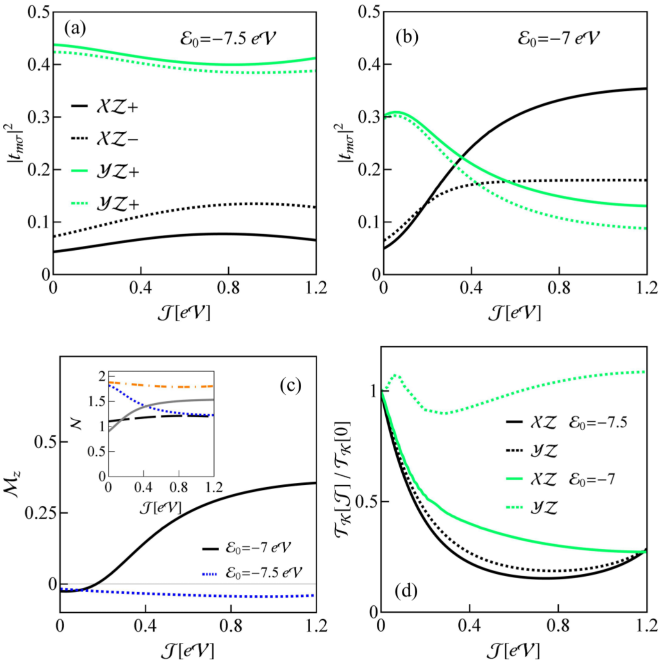

FIG. 15. (Color online) Dependence of the Kondo state characteristics on the value of exchange parameter: (a), (b) Slave boson expectation values $|t_{m\sigma}|^2$ for $\mathcal{N} \approx 3$ ($\varepsilon_0 = -7.5$ eV) and $\mathcal{N} \approx 2.7$ ($\varepsilon_0 = -7$ eV), $\mathcal{E}_F = -0.8$. (c) Magnetic moments of Co impurity. Inset shows orbital occupancies: for $\varepsilon_0 = -7.5$ dashed line ($\mathcal{N}_{yz}$) and dash-dotted line ($\mathcal{N}_{xz}$), $\varepsilon_0 = -7$ solid line ($\mathcal{N}_{yz}$) and dotted line ($\mathcal{N}_{xz}$). (d) Relative quasiparticle temperatures.

Figure 15 illustrates the impact of Hund's coupling on Kondo physics. We show two examples $\mathcal{N} \approx 3$ and $\mathcal{N} \approx 2.7$. Insight on the slave boson dependencies and orbital occupancies highlights the stronger impact of Hund's coupling for $\mathcal{N} \approx 2.7$. In this case a remarkable weakening of Kondo screening is observed for high values of exchange coupling (increase of magnetic moment). In general one can expect that an increase of magnetic correlations with the increase of exchange coupling should result in a decrease of Kondo temperature, as a consequence of competitiveness of different correlations. The spin and orbital degrees of freedom fluctuate less freely in this case. This general tendency is really observed in most presented cases. For reduced occupancy, however, the $\mathcal{N} \approx 2.7$ characteristic temperature T_K^{yz} changes nonmonotonically, which is reflected in change of partial occupancy from slightly below half filling to values above. For $\mathcal{N}_{yz} = 1$ a maximum of the Kondo temperature is observed.

D. Charge fluctuation effects: NCA and EOM approaches

The SBMFA results become worse with increasing temperature due to fluctuations. Some account of fluctuations is achieved by systematic corrections to the MFA approach using, e.g., hybridization expansion or applying the equation-of-motion method. In this section we briefly analyze the role of charge fluctuations in the considered many-body processes. For transparency of considerations we discuss only the case when the chemical potential is located not too close to any VH singularity. We limit ourselves to the lowest order in hybridization self-consistent approximation NCA and EOM with Lacroix's decoupling approximation [51]. These methods apply for higher temperatures, but they give reliable results also down to a fraction of $T_{\mathcal{K}}$ [48,53,55]. They fail however for $T \ll T_{\mathcal{K}}$, but in this range in turn SBMFA is valid.

Despite the low-temperature deficiencies the use of these impurity solvers allows us to get a crude insight into the full spectrum of the one-particle Green's functions and not just the quasiparticle contribution. In the present work we apply the NCA method for finite $\mathcal{U}$ [57–60]. In NCA one takes into account only diagrams without noncrossing of substrate electron lines, which correspond to simple hopping processes, where electron or hole hops into the adatom at some time and then out at a later time. This leads to a set of NCA integral equations for the fixed occupation self energies:

$$\begin{aligned}
\Sigma^{(0)}(z) &= \sum_{m\sigma} \int \frac{d\varepsilon}{\pi} \Delta_{m\sigma}(\varepsilon) f(\varepsilon) \mathcal{G}^{(1)}_{m\sigma}(z+\varepsilon),\\
\Sigma^{(1)}_{m\sigma}(z) &= \int \frac{d\varepsilon}{\pi} \left[\Delta_{m\sigma}(\varepsilon) f(-\varepsilon) \mathcal{G}^{(0)}(z-\varepsilon) + \Delta_{m\overline{\sigma}}(\varepsilon) f(\varepsilon) \mathcal{G}^{(2)}_{m\sigma m\overline{\sigma}}(z+\varepsilon) + \sum_{\sigma'} \Delta_{\overline{m}\sigma'}(\varepsilon) f(\varepsilon) \mathcal{G}^{(2)}_{m\sigma\overline{m}\sigma'}(z+\varepsilon) \right],\\
\Sigma^{(2)}_{m\sigma m'\sigma'}(z) &= \int \frac{d\varepsilon}{\pi} \Bigg[\Delta_{m\sigma}(\varepsilon) f(-\varepsilon) \mathcal{G}^{(1)}_{m'\sigma'}(z-\varepsilon) + \Delta_{m'\sigma'}(\varepsilon) f(-\varepsilon) \mathcal{G}^{(1)}_{m\sigma}(z-\varepsilon)\\
&\quad + \begin{cases} \Delta_{m'\overline{\sigma'}}(\varepsilon) f(\varepsilon) \mathcal{G}^{(3)}_{m\sigma}(z+\varepsilon) + \Delta_{m\overline{\sigma}}(\varepsilon) f(\varepsilon) \mathcal{G}^{(3)}_{m'\sigma'}(z+\varepsilon), & m \neq m'\\ \sum_{\sigma} \Delta_{\overline{m}\sigma}(\varepsilon) f(\varepsilon) \mathcal{G}^{(3)}_{\overline{m}\sigma}(z+\varepsilon), & m = m' \end{cases} \Bigg],\\
\Sigma^{(3)}_{m\sigma}(z) &= \int \frac{d\varepsilon}{\pi} \left[\Delta_{m\sigma}(\varepsilon) f(-\varepsilon) \mathcal{G}^{(2)}_{\overline{m\sigma}\,\overline{m\sigma}}(z-\varepsilon) + \sum_{\sigma'} \Delta_{\overline{m}\overline{\sigma'}}(\varepsilon) f(-\varepsilon) \mathcal{G}^{(2)}_{m\sigma\overline{m}\sigma'}(z-\varepsilon) + \Delta_{m\overline{\sigma}}(\varepsilon) f(\varepsilon) \mathcal{G}^{(4)}(z+\varepsilon) \right],\\
\Sigma^{(4)} &= \sum_{m\sigma} \int \frac{d\varepsilon}{\pi} \Delta_{m\overline{\sigma}}(\varepsilon) f(-\varepsilon) \mathcal{G}^{(3)}_{m\sigma}(z-\varepsilon),
\end{aligned} \tag{8}$$

where $\mathcal{G}^{(p)}_{m\sigma}(z) = [z - \mathcal{E}_{(p)} - \Sigma^{(p)}_{m\sigma}(z)]^{-1}$ ($p = 1{,}3$ with energies $\mathcal{E}_{(1)} = \varepsilon_0$ and $\mathcal{E}_{(3)} = 3\varepsilon_0 + 3\mathcal{U}$) and $\mathcal{G}^{(2)}_{m\sigma m\overline{\sigma}}(z) = [z - \mathcal{E}_2 - \Sigma^{(2)}_{m\sigma m\overline{\sigma}}(z)]^{-1}$ ($\mathcal{E}_2 = 2\varepsilon_0 + \mathcal{U}$), $\mathcal{G}^{(4)}(z) = [z - \mathcal{E}_4 - \Sigma^{(4)}(z)]^{-1}$ (where $\mathcal{E}_4 = 4\varepsilon_0 + 6\mathcal{U}$) are pseudoparticle fermion and boson propagators. Fermion resolvents correspond to odd occupancies of adatom and boson to even. $f(\varepsilon)$ is the Fermi distribution function and $\Delta_{m\sigma}(\varepsilon) = -\mathrm{Im}[\Sigma_{m\sigma}(\varepsilon)]$. The retarded local Green's functions may be evaluated by analytic continuation from the corresponding imaginary time propagator and can be expressed as convolution of pseudoparticle Green's functions:

$$\begin{aligned}
\mathcal{G}_{m\sigma}(i\omega) = (1/\mathcal{Z}) \oint_{\mathcal{C}} \frac{dz}{2\pi i} e^{-z/(k_B T)} \Bigg[&\mathcal{G}^{(0)}(z) \mathcal{G}^{(1)}_{m\sigma}(z+i\omega) + \mathcal{G}^{(1)}_{m\overline{\sigma}}(z) \mathcal{G}^{(2)}_{m\sigma m\overline{\sigma}}(z+i\omega) + \sum_{\sigma'} \mathcal{G}^{(1)}_{\overline{m}\sigma'}(z) \mathcal{G}^{(2)}_{m\sigma\overline{m}\sigma'}(z+i\omega)\\
&+ \sum_{\sigma'} \mathcal{G}^{(2)}_{m\overline{\sigma}\overline{m}\sigma'}(z) \mathcal{G}^{(3)}_{\overline{m}\sigma'}(z+i\omega) + \mathcal{G}^{(2)}_{\overline{m}\sigma\overline{m}\overline{\sigma}}(z) \mathcal{G}^{(3)}_{m\sigma}(z+i\omega) + \mathcal{G}^{(3)}_{m\overline{\sigma}}(z) \mathcal{G}^{(4)}(z+i\omega) \Bigg],
\end{aligned} \tag{9}$$

where $\mathcal{Z}$ is the impurity partition function; i.e.,

$$\begin{aligned}
\mathcal{Z} = \oint_{\mathcal{C}} \frac{dz}{2\pi i} e^{-z/(k_B T)} \Bigg[&\mathcal{G}^{(0)}(z) + \sum_{m\sigma} \mathcal{G}^{(1)}_{m\sigma}(z)\\
&+ \sum_{m\sigma m'\sigma'} \mathcal{G}^{(2)}_{m\sigma m'\sigma'}(z) + \sum_{m\sigma} \mathcal{G}^{(3)}_{m\sigma}(z) + \mathcal{G}^{4}(z) \Bigg].
\end{aligned} \tag{10}$$

It is known that noncrossing approximations encounter difficulties in the case of broken symmetry, which can produce at low temperatures spurious peaks in DOS [54], but we have not observed such artifacts for the examined case. The complementary method we use, EOM, consists in differentiating the Green's functions with respect to time which generates the hierarchy of equations with higher order GFs (11). For the discussed $\mathcal{N} = 3$ case apart from single- and two-electron also three- and four-particle Green's functions play a role. In order to truncate the series of EOM equations, we use the generalized procedure proposed by Lacroix [51], which approximates the GFs involving two conduction electron operators by single-particle correlations and the corresponding Green's function of lower order:

$$\begin{aligned}
\langle\langle c^{+}_{kn\overline{\sigma}} c_{qn\sigma} d_{m'\overline{\sigma}} \mathcal{O}; d^{+}_{m\sigma} \rangle\rangle &\simeq -\langle c^{+}_{kn\overline{\sigma}} d_{m'\overline{\sigma}} \rangle \langle\langle c_{qn\sigma} \mathcal{O}; d^{+}_{m\sigma} \rangle\rangle,\\
\langle\langle c^{+}_{kn\overline{\sigma}} d_{m\sigma} c_{qn\overline{\sigma}} \mathcal{O}; d^{+}_{m\sigma} \rangle\rangle &\simeq -\langle c^{+}_{kn\overline{\sigma}} c_{qn\overline{\sigma}} \rangle \langle\langle d_{m\sigma} \mathcal{O}; d^{+}_{m\sigma} \rangle\rangle,\\
\langle\langle d^{+}_{m'\overline{\sigma}} c_{qn\sigma} c_{kn\overline{\sigma}} \mathcal{O}; d^{+}_{m\sigma} \rangle\rangle &\simeq -\langle d^{+}_{m'\overline{\sigma}} c_{kn\overline{\sigma}} \rangle \langle\langle c_{qn\sigma} \mathcal{O}; d^{+}_{m\sigma} \rangle\rangle,\\
\langle\langle c^{+}_{qn\overline{\sigma}} c_{kn\overline{\sigma}} d_{m\sigma} \mathcal{O}; d^{+}_{m\sigma} \rangle\rangle &\simeq +\langle c^{+}_{qn\overline{\sigma}} c_{kn\overline{\sigma}} \rangle \langle\langle d_{m\sigma} \mathcal{O}; d^{+}_{m\sigma} \rangle\rangle,
\end{aligned} \tag{11}$$

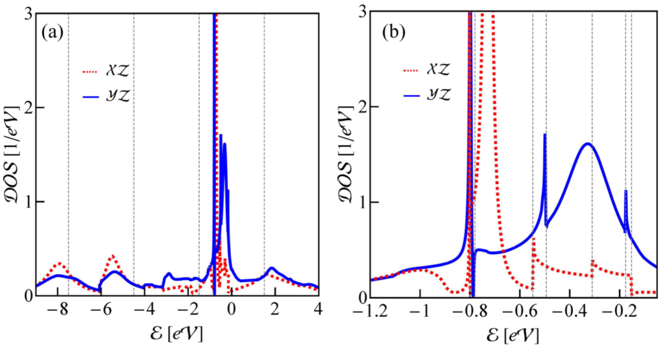

FIG. 16. (Color online) Comparison of xz (dotted line) and yz (solid line) contributions to the DOS of Co adatom in h_1 position of 4ZGNR ($\mathcal{E}_{\mathcal{F}} = -0.8$) (NCA). The vertical dashed lines in (a) determine the positions of bare Coulomb peaks and in (b) the positions of singularities in the interacting self-energies.

where $m' = xz(yz)$ and $\mathcal{O} = 1, n_{m_1\sigma_1}, n_{m_1\sigma_1}n_{m_2\sigma_2}$. The correlations $\langle c^{+}_{kn\sigma} d_{m'\sigma}\rangle$ and $\langle c^{+}_{kn\sigma} c_{qn\sigma}\rangle$ occurring in Eq. (11) play the leading role in the Kondo effect. Upon calculating these averages self-consistently using the spectral theorem and corresponding Green's functions the EOM set is closed and can be therefore solved. For detailed analysis of EOM hierarchy and decoupling schemes, see, e.g., Refs. [52,53]. The one-particle NCA spectrum is assembled in Fig. 16. For the assumed position of the Fermi level ($\mathcal{E}_{\mathcal{F}} = -0.8$ eV) the main contribution comes from convolution of $\mathcal{G}^{(2)}$ and $\mathcal{G}^{(3)}$ functions. In addition to the many-body resonances located around $\mathcal{E}_{\mathcal{F}}$, also charge fluctuation peaks are visible reflecting fluctuations into fully, doubly, singly occupied and empty $\{d_{xz}, d_{yz}\}$ shell. Their positions are renormalized and the peaks are broadened as a result of combined effect of hybridization and many-body correlations. The Coulomb peaks are only weakly temperature dependent, whereas significant temperature evolution of many-body resonances is observed [Figs. 17(a) and 17(b)]. The energy scales of spin-orbital fluctuations and charge fluctuations are not well separated and especially ($\mathcal{N} = 3$, $\mathcal{N} = 4$) Coulomb resonances strongly perturb quasiparticle resonances. The singularities of the nanoribbon spectrum can influence the physics around Fermi level despite the fact that they are not located close to $\mathcal{E}_{\mathcal{F}}$. The observed dips are not direct traces of singularities of hybridization function; they reflect singularities of interacting self-energies, which describe repeated conversion of doubly (triple) occupied impurity into single and triple (double and fully) occupied adatom by emitting or absorbing nanoribbon electron. The singularities of interacting self-energies however have as a source corresponding Van Hove singularities of density of states. Tracing formal generation of singularities via Eq. (8) one can point out these connections. For example one can identify that singularities at $\mathcal{E} = -0.79$ eV and $\mathcal{E} = -0.78$ eV originate from VH3v of the hybridization function; those at $\mathcal{E} = -0.55$ eV and $\mathcal{E} = -0.5$ eV come from the VH3c singularity; and at $\mathcal{E} = -0.31$ eV and $\mathcal{E} = -0.18$ eV in turn from VH4v, etc. [see Figs. 7(b) and 16(b)]. The main features of the EOM spectrum are similar to NCA results. Charge fluctuation peaks show up more clearly in EOM and the observed impact of charge fluctuation peaks next to the Fermi level on the many-body resonances is stronger than in NCA. Similarly to NCA calculations also in EOM density of states a dip introduced by interacting self-energies, being a reminiscence of the singularity of the nanoribbon electronic structure, is visible. The sharp dips appearing in the presented spectra would certainly be partially smoothed out if finite-lifetime effects were taken into account, similarly to the presented temperature effects [Figs. 17(a) and 17(b)]. This remark concerns mainly the impact of singularities on interacting self-energies, because they probe also electrons away from the Fermi level. In some cases, in addition to the dips, peculiarities of electronic structure of the host are reflected also as additional peaks in the spectral function of the impurity (see the peak slightly above the Fermi level in EOM and NCA Co densities of states, Fig. 17). This structure is due to a new pole of the Green's function: intersection of the $\omega - \varepsilon_0$ line with the real part of self-energy. The real part of interacting self-energy dramatically changes between singularities taking values from a wide range of energy and thus the mentioned intersection is likely in this interval. The occurrence of additional many-body structures is a combined effect of correlations and singularities of nanoribbon DOS. In order to elucidate this point we present in Fig. 18(a) comparison of DOS calculated in EOM considering the case of inclusion of dynamical correlations (Lacroix's decoupling) or neglect of correlations ($\langle c^{\dagger}_{kn\sigma} d_{m\sigma}\rangle = 0$), as well as comparing densities of states calculated with hybridization function from DFT with the results, where energy-independent hybridization has been assumed. An additional peak above $\mathcal{E}_{\mathcal{F}}$ is only found when both correlations and full structure of hybridization

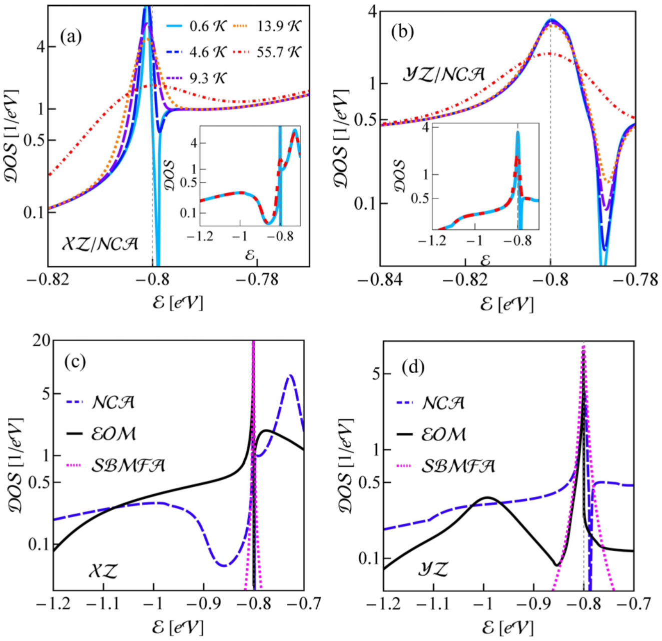

FIG. 17. (Color online) Density of states of Co impurity at h_1 position ($\mathcal{E}_{\mathcal{F}} = -0.8$). (a), (b) Temperature evolution of orbital partial densities of states calculated with the use of NCA approximation (insets are the extended views for $T = 0.6$ K and 55.7 K). (c), (d) Comparison of NCA DOS with EOM spectra and SBMFA densities of states.

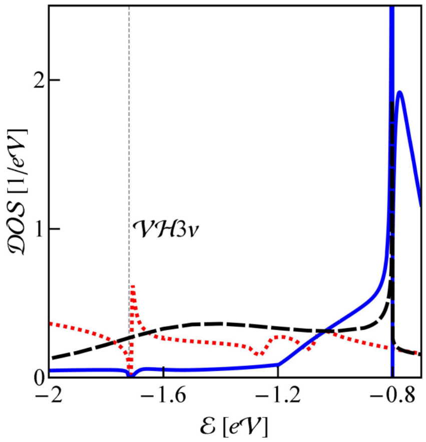

FIG. 18. (Color online) Partial xz DOS of Co adatom calculated by EOM with realistic (DFT) hybridization function of 4ZGNR with Lacroix's decoupling (solid blue line), without dynamical correlations (red dotted line). Dashed black curve presents the corresponding DOS calculated with Lacroix's decoupling, but using energy-independent, constant hybridization function.

function are taken into account. The interesting problem of the enriched structure of many-body resonances resulting from peculiarities of electronic structure of the host has been only announced here and we leave a more detailed analysis of this problem as an open question for future study.

IV. CONCLUSIONS

The issue of geometrical and electric control of magnetic properties of the Kondo impurity on an ultranarrow zigzag graphene nanoribbon via peculiarities of its electronic structure discussed in the present paper is of potential importance for spintronics. Experiments on Kondo physics in graphene nanoribbons are still missing, but we believe that the results presented in this paper will stimulate the experimental effort in this direction. The presented scheme of calculations, which is similar to some other slightly different earlier approaches [46,47,94,95], combines the first-principles calculations with the addition of missing correlations by a Hubbard-type term and next solving the many-body problem by the well-known impurity solvers. The basic input quantity for many-body analysis - the hybridization function, is determined by impurity matrix hopping amplitudes and local nanoribbon DFT Green's functions, both quantities achievable from most output files of DFT programs (e.g., in the VASP code almost directly from the PROCAR file).

We have shown that the Kondo effect of the Co impurity in graphene nanoribbons is controlled not only by spin but also by the orbital degrees of freedom. Our DFT analysis indicated that only two from five d orbitals are responsible for magnetic properties of the Co impurity. For the preferred hollow positions of the Co atom and chemical potential lying in the vicinity of the gap this role is played by d_{xz}, d_{yz} orbitals. In the nanoribbon the C_{6v} symmetry of pure graphene is broken and d_{xz} and d_{yz} couple differently to the nanoribbon matrix. The presence of the edge states in ZGNR introduces local magnetic polarization close to the edge and consequently breaks also impurity spin degeneracy in this region. The electronic structure of ZGNR is rich in Van Hove singularities and this property can be exploited for electric control of magnetic properties. If the Fermi level crosses the singularities the drastic changes of hybridization functions result which in turn reflect in strong variation of many-body resonances, leading in some cases to transition from Kondo-like behavior into mixed valence or even resulting in complete destroying of resonances. For symmetry reasons the specific singularity exhibits differently in different spin and orbital channels and therefore not all channels are equally influenced by its presence. Crossing the singularity by the Fermi level results in some cases in an interchange of the roles of orbitals or spins leading to reversal of spin or orbital pseudospin. Since the chemical potential can be shifted by gate voltage, this opens a path of electric field control of these properties. Our present study shows that the unconventional electronic and magnetic features of zigzag graphene nanoribbons not only raise new fundamental issues in many-body physics of adatoms, but also that ZGNRs with impurities can be promising objects for potential applications in spintronics.

A key question concerns the capability to make measurements of the described effects. To check our predictions experimentally, the detection methods of sufficient subnanometer spatial resolution together with single-spin sensitivity are required. It has been proved for many systems that using atomic force microscopy a controllable move of a single atom and its deposition in a selected position on the surface is possible [29,30,96]. This gives us hope that a similar adatom site engineering in graphene nanostructures is also within reach of present-day technique. The Kondo effect has been observed by STM spectroscopy for many impurities on different surfaces [97–99], including graphene [40], but experiments on Kondo physics in graphene nanoribbons are still missing. Since no fundamental principle precludes such measurements, we believe that they will be performed in the near future. Kondo temperatures can be extracted from the half-widths of STM lines. Typically the STM spectra of Kondo resonances on metallic substrates display Fano profiles [99] resulting from the interference between the direct paths from the tip to the host and those via many-body state of impurity. In graphene nanoribbons, the situation is complicated, because similarly to the earlier presented pronounced energy dependence of hybridizations (with VH anomalies in the low-energy range), analogous energy dependencies are expected for tip-ZGNR mixing functions, which should have a strong impact on interference conditions. Our preliminary results show that the STM picture of the adatom at a given site can change by shifting the chemical potential from Fano-like line shape to Kondo-like. The spin-dependent features of Kondo resonances [e.g., map in Fig. 13(b)] should be possible to observe by spin-polarized scanning tunneling microscopy (SP-STM) [92]. In particular, a huge change of spin polarization expected for example for the h_1 site when the chemical potential crosses the VH singularity [Fig. 12(c)] should be detectable by a drastic change of spin-polarized STM contrast. Similar changes of orbital polarizations [Figs. 10(c) and 12(a)] are much more difficult to observe experimentally, but considerable variation of orbital polarization of STM spectra should be visible with a change of tip-adatom distance, because different symmetries of adatom resonances have different space dependence in the vertical direction. For orbital symmetries of the same vertical dependencies (e.g., d_{xz} and d_{yz}) presumably the same role would be played by horizontal STM probing in the close tip-substrate distance range. In analogy to spin-polarized tips, the orbitally polarized tips (tip apex characterized by different orbital occupations of states) can allow orbital selectivity. As far as we know, such experiments have not yet been carried out. The theoretical basis of STM measurements of transition-metal (TM) impurities on graphene nanoribbons requires detailed examination; this is currently analyzed and will be soon published. One of the interesting results presented by us was a decrease of efficiency of Kondo screening near the singularities, i.e., increase of effective magnetic moment and possible flips of partially screened magnetic moments in this range. The changes of magnetic moments are associated with the variation of spin polarizations [Figs. 12(c) and 12(d)] and in this sense SP-STM spectroscopy also detects these changes, but it does not give information on the moments themselves. Magnetic moments depend on the total adatom density of states and this is not probed by this technique. A promising method for single spin detection is magnetic resonance force microscopy (MRFM) [100,101], where the information of the spin state is transferred to the state of the driven cantilever with a small magnetic material on its tip. We expect that the aforementioned gate-induced magnetic moment flips near singularities should be observed by a phase shift of the oscillation of the cantilever, monitored by an optical interferometer. Given the steady improvement in experimental technique, the measurements of this type will certainly be soon possible. Similar effects, but induced by transverse time dependent magnetic field (cyclic adiabatic inversion), have been already reported [101].

ACKNOWLEDGMENTS

This work was supported by the Polish Ministry of Science and Higher Education as Research Project No. N N202 199239 for the years 2010-2013. Two of us (D.K. and J.K.) would like also to thank for support the Institute of Molecular Physics, Polish Academy of Sciences, under an internal grant for Young Scientists.

APPENDIX A: ADSORPTION ENERGIES AND MAGNETIC MOMENTS: COMPARISON OF DFT AND GGA+U RESULTS

Figure 19(a) shows the DFT total energy curves for different positions of adatom. Similarly as in graphene [46], our DFT study indicates that the Co adatom in ZGNRs prefers hollow sites. In these positions, the coordination number is maximized and the impurity is not associated with a particular sublattice, but instead binds three carbon atoms from each. Since nanoribbon polarization is nonuniform, adsorption energy also depends on Co spin polarization, but as shown in the example of the h_1 position [inset of Fig. 19(a)], the adsorption curves for different spin orientations do not differ significantly. Nevertheless the predicted spin orientations of Co adatoms deposited at the h_1 and h_3 positions of 4ZGNR are opposite, whereas at the ribbon center (h_2), where no net magnetic polarization of ZGNR occurs, the energies for both Co spin orientations are degenerate. We have also checked that within DFT, hollow sites are also preferred for Co in armchair nanoribbons. In pure graphene not only cobalt, but also other 3d adatoms including Fe and Ni were predicted to adsorb in this position [73,102]. This fact was explained as a result of the negligible role played by s orbitals in binding energy at this site, due to their decoupling from the low-energy states, which is forced by symmetry [104]. In nanoribbons the hexagonal symmetry is broken, but still in the low-energy range only weak coupling with s orbitals is observed. Following Power *et al.* [33] we have also checked that at the edge a new type of metastable adsorption site is realized (h_0, Fig. 1), where impurity connects to three edge zigzag atoms. This position is however only reached after relaxation along the path starting from the adatom originally siting at the t_1 or t_2 positions.

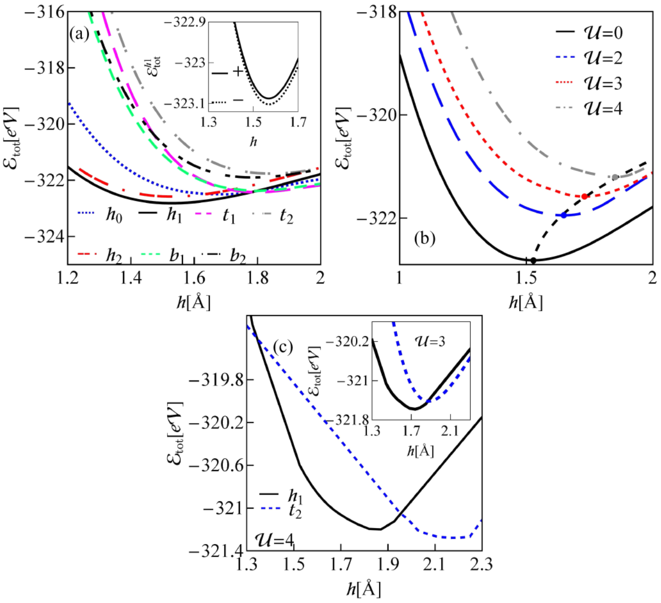

FIG. 19. (Color online) (a) LDA total energy curves for different positions of Co adatom on 4ZGNR. Inset is the zoom view of spin-resolved energy curves for h_1 position presented close to minimum. (b) GGA+U total energy curves for h_1 position for selected values of U. (c) Comparison of GGA+U energy curves for LS (h_1) and HS (t_2) states for $\mathcal{U} = 4$ eV and in the inset for $\mathcal{U} = 3$ eV.

In Sec. IIC we have illustrated the role of d_{xz} and d_{yz} orbitals in forming the magnetic moment of Co at hollow sites of ZGNR. We have examined that the same pair of orbitals plays also the role of magnetic orbitals in AGNRs, independent of the distance from the edge. Bearing in mind that due to C_{6v} symmetry this pair of orbitals (E_1) plays the dominant role in forming magnetic moments of Co in hollow positions also in pure graphene [46], one can conclude that symmetry-breaking perturbations introduced by nanoribbon edges are not strong enough to destroy the picture of magnetic dominance of E_1 orbitals at hollow sites of nanoribbons. Similarly as in graphene, the crystal field acting on Co in hollow positions in ZGNRs is such that d_{xz} and d_{yz},orbitals are partially occupied. It seems that this situation persists also in some other TM atoms. We have performed some testing DFT calculations for selected atoms, which confirm the dominant role of this pair of orbitals in magnetic properties of impurities, especially for atoms with high electron filling of the d shell, but often contributions of other orbitals to magnetic moment are also not negligible. The total magnetic moment of Fe for example at h_1 site of 4ZGNR is 2.346 μ_B (in pure graphene 2.00 μ_B [103]) with 0.781 and 0.810 contributions of d_{xz} and d_{yz}, respectively. The d electron occupation of Fe ($\mathcal{N}_d^{\rm Fe} = 6.46$) is smaller than in Co and in this case also d_{xy} and $d_{x^2-y^2}$ minority spin orbitals are partially shifted above $\mathcal{E}_{\mathcal{F}}$ contributing to magnetic moment 0.396 and 0.346, respectively. For Ni with still higher d-electron filling ($\mathcal{N}_d^{\rm Ni} = 8.56$), the magnetic moment at the h_1 position of 4ZGNR is small (0.22 μ_B, with contribution of 0.12 from d_{yz} and residual almost equal shares from the d_{xz}, d_{xy}, and $d_{x^2-y^2}$ orbitals). At the h_2 site the magnetic moment of Ni vanishes, similarly as in the case of pure graphene [103]. To get an insight into the case of an atom with less than half filling of the d shell, we have checked vanadium ($\mathcal{N}_d^{V} = 3.95$) with magnetic moment 3.1 μ_B (magnetic moment of V in graphene is 3 μ_B [103]). For V all d orbitals have their spin minority components partially shifted above $\mathcal{E}_{\mathcal{F}}$ and they all contribute to the magnetic moment ($\mathcal{M}_{z^2} = 0.97$, $\mathcal{M}_{xz} = 0.53$, $\mathcal{M}_{yz} = 0.23$, $\mathcal{M}_{xy} = 0.73$, $\mathcal{M}_{x^2-y^2} = 0.56$). For all considered TM adatoms the electron transfer from their 4s orbitals to 3d orbitals is observed; in the case of atoms from the top of the series (Fe, Co, Ni) this leads to reduction of magnetic moments, whereas for vanadium, which represents the lower part of series, an increase of magnetic moment in comparison to the free atom value results.

It is well known that adsorption geometries can be very sensitive to the effects of correlations [104]. The adsorption is governed by contributions to chemical bonding from s against those from d orbitals. Coulomb repulsion suppresses the role of d orbitals in chemical bonding [89,104]. Figure 19(b) presents examples of total energy curves of Co placed in the h_1 position obtained within the GGA+U type approach. The estimated adsorption energy significantly lowers with the increase of $\mathcal{U}$, taking for $\mathcal{U} = 3$ eV values -1.16 and -0.87 eV for the h_1 and h_2 positions, respectively, compared with corresponding DFT values -1.39 and -1.25 eV. The inset of Fig. 19(b) compares the height dependencies of magnetic moments for $\mathcal{U} = 0$ and $\mathcal{U} = 2$ eV. The increase of the overlap of impurity to ribbon states with the decrease of vertical distance results in a reduction of magnetic moment. Close to the nanoribbon surface the occupation of weakly hybridized 4s states is less favorable than these of strongly hybridizing 3d orbitals. Hybridization lowers the energy of the orbitals and due to increased delocalization, the Coulomb repulsion is reduced. In consequence of the 4s-3d charge transfer also the observed decrease of magnetic moment results. We also show that similarly to the analogous calculations for pure graphene [46], the Coulomb interaction contribution to the adsorption energy can change the preference of impurity sites. It is illustrated in Fig. 19(c), which compares Co adatom potential energy curves for high-spin state (HS, $\mathcal{S} = 3/2$) (t_2 position) and low spin (LS, $\mathcal{S} = 1/2$) (h_1 position) calculated for $\mathcal{U} = 2$ eV and $\mathcal{U} = 4$ eV. As is seen, GGA+U calculations predict a shift of global minimum from LS to HS state, which is associated with the change of the preferred site and an increase of equilibrium vertical position of the adatom. The energy difference of minima for these two electronic states for $\mathcal{U} = 4$ eV is ~0.1 eV and is smaller than the corresponding value in pure graphene (0.2 eV [46]). More realistic estimations should take into account the height dependence of effective Coulomb interaction caused by a change of screening processes [104]. It is expected that effective Coulomb interaction is reduced close to the carbon surface, due to increase of delocalization. One can conclude that DFT results should be treated with caution, only as a good approximation in the restricted range of low vertical distance of adatom from nanoribbon plane. It is not resolved yet which of the configurations is closer to experiment, but even supposing that the LS state of the Co adatom is only a local minimum, the energy barrier between the minima (~0.12 eV) is high enough to trap the adatom at this position at low temperatures. In the present paper we restricted ourselves to a discussion of Kondo physics only at hollow positions (spin-orbital $\mathcal{S} = 1/2$ Kondo effect). The Kondo screening of the high-spin case would run by a completely different scenario [46]. It is worth mentioning that there are examples where both LDA and GGA+U calculations are consistent and predict the same hollow site adsorption. This is the case for, e.g., NiH impurity [104], which has an electronic configuration like Co discussed here, and therefore the present calculations can be indirectly addressed also to this system.

The Coulomb interaction parameter is also essential for an estimation of magnetic moments, because it greatly affects the orbital arrangements above $\mathcal{E}_{\mathcal{F}}$. This is illustrated in Fig. 20, where we additionally show the effect of Hund's coupling. Coulomb interaction enhances the magnetic moment of the Co adatom at ZGNR and $\mathcal{J}$ reduces it. In the inset of Fig. 20 we show magnetic moment dependencies of the Co atom on the height for three values of $\mathcal{U}$. Increase of the overlap of impurity to ribbon states with the decrease of the vertical distance results in a reduction of magnetic moment. Close to the nanoribbon surface the occupation of weakly hybridized 4s states is less favorable than those of strongly hybridizing 3d orbitals. Hybridization lowers the energy of the orbitals and due to increased delocalization the Coulomb repulsion is reduced. In consequence of 4s-3d charge transfer the decrease of magnetic moment results; for finite $\mathcal{U}$ the vanishing of

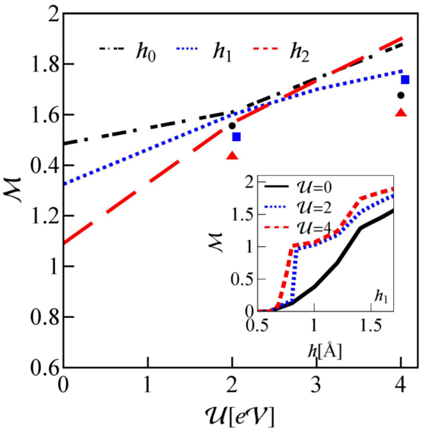

FIG. 20. (Color online) GGA+U estimations of total magnetic moment of Co impurity in 4ZGNR for different values of Coulomb interaction parameter $\mathcal{U}$. Inset shows magnetic moment of Co placed at h_1 position of 4ZGNR at a distance h from the nanoribbon plane. The dots represent additional effect of exchange $\mathcal{J} = 0.9$ eV for h_0 (circle), h_1 (square), and h_2 (triangle).

magnetic moment with lowering of the distance from the ribbon plane proceeds rapidly.

APPENDIX B: VARIATION OF KONDO TEMPERATURE WITH NANORIBBON WIDTH

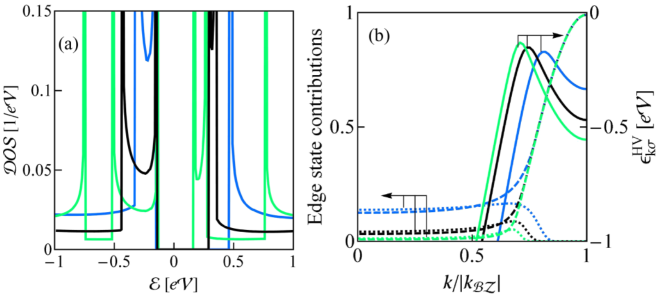

FIG. 21. (Color online) (a) Density of states of NZGNR: $N = 4$ (blue line/gray line), $N = 8$ (black), $N = 14$ (green/light gray line). (b) Highest valence bands (HV) of NZGNR ($\varepsilon^{HV}_{k\sigma}$) (solid lines, right axis of ordinates) and the corresponding edge state contributions $|\langle p^{A_1}_{z\sigma}|k\sigma^{HV}\rangle|^2$ (dashed lines for spin up and dotted lines for spin down, left axis of ordinates). Assignment of the line colors to the ribbon widths is the same as in (a).

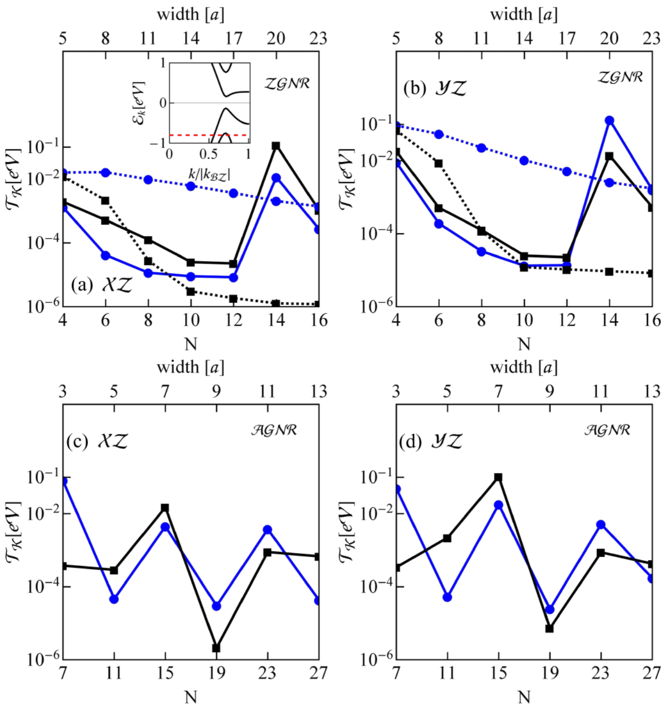

FIG. 22. (Color online) Characteristic quasiparticle temperatures $T_{\mathcal{K}}$ of Co in NZGNR [(a), (b)] and NAGNR [(c), (d)] for xz [(a), (c)] and yz [(b), (d)] channels. Dots represent the results for central hollow location (h_c) and squares for hollow positions next to the edge (h_1). Dotted lines correspond to $\mathcal{E_F} = -0.25$ eV case and solid lines to $\mathcal{E_F} = -0.8$ eV. Inset of (a) is a zoom picture of the band structure of 14ZGNR and illustrates a crossing of the Fermi level ($\mathcal{E_F} = -0.8$ eV) by the next valence band. The upper horizontal axes show the nanoribbon widths expressed in graphene lattice constant units a ($a = 1.42$ Å).

Here we give some examples of Kondo temperatures of the Co adatom for nanoribbons of different widths. For brevity, instead of showing all the orbital- and spin-dependent hybridizations, we present as an assisting picture only the width evolution of total density of states of NZGNR [Fig. 21(a)]. In wider ZGNRs the interactions between the edge states are less pronounced, staggered sublattice potentials weaken, band gaps decrease, and a reduction of DOS in the examined low-energy range is observed. Correspondingly decrease also hybridization functions (not shown), and this leads to an overall drop of $T_{\mathcal{K}}$ with the increase of N. Apart from this general tendency the modifications of Kondo temperature depend on the position of chemical potential with respect to singularities. To focus our attention, let us restrict ourselves to only two representative positions of Fermi energies $\mathcal{E_F} = -0.25$ and $\mathcal{E_F} = -0.8$ eV. The former point lies in the energy range between the two Van Hove singularities (VH1ν and VH2ν) and the latter is chosen more distant from any singularity. For $\mathcal{E_F} = -0.25$ eV the edge states dominantly contribute to the band structure [Fig. 21(b)] and correspondingly these states play the crucial role in hybridization functions. For h_1 hybridization is mainly due to edge states and Kondo temperature in this case is higher than in the center of the ribbon [$T_{\mathcal{K}}(h_1) > T_{\mathcal{K}}(h_c)$]. The edge contribution decreases when one moves towards the center of the ribbon and the $T_{\mathcal{K}}(h_c)$ curve drops with the increase of N much faster than $T_{\mathcal{K}}(h_1)$. Comparing the evolutions of Kondo temperatures for these two types of sites it is important to remember that we monitor the central site, which is more and more distant from the edge with the increase of N. For $\mathcal{E_F} = -0.8$ eV the role of edge states is nonsignificant [Fig. 21(b)] and the central and edge hybridizations do not differ so drastically in this case, which is reflected in the smaller differences of Kondo temperatures for edge and central positions. For $\mathcal{E_F} = -0.8$ eV the Kondo temperature for the h_1 site is smaller than for h_c and this can be attributed to different manifestation of VH2ν singularity in both cases. It is slightly surprising that despite the location of the singularity far away from the considered energy, still its considerable impact on many-body resonance is observed [compare Figs. 11(a) and 13(c)]. In the h_1 position [Fig. 13(c)] a dip in the DOS is seen for energy corresponding to VH2ν, which effectively narrows the resonance, whereas for the central position [Fig. 11(a)] the influence of VH2ν is only minor at least for the yz sector. Of interest is also the observed nonmonotonic behavior of characteristic temperatures with N. The jump for $N = 14$ is a consequence of entering of the next band on the Fermi level [see the inset of Fig. 22(a)], which is equivalent to locating of the VH3ν singularity at $\mathcal{E} \approx -0.75$ eV [Fig. 21(a)]. Since the role of edges is different in zigzag and armchair nanoribbons [105], we also show for comparison in Figs. 22(c) and 22(d) a few examples of width dependence of cobalt Kondo temperature for armchair graphene nanoribbons. The differences between central-hollow and edge-hollow cobalt Kondo temperatures are smaller for AGNR due to the absence of edge states in this structure. The band structure of GNRs is strongly influenced by quantum confinement effects. It is known that distinctively different confinement conditions for ribbon widths $N = 3p$, $3p + 1$, and $3p + 2$ (p is an integer) are reflected, e.g., in separation of gap size hierarchy for different categories and varied forms of the eigenfunctions with energies close to the gap [105]. In the examined dependencies this fact is reflected in the oscillatory character of the $T_K(N)$ decay with N. More details will be discussed in a forthcoming publication.

[1] K. S. Novoselov, A. K. Geim, S. V. Morozov, D. Jiang, Y. Zhang, S. V. Dubonos, I. V. Grigorieva, and A. A. Firsov, Science **306**, 666 (2004).

[2] A. K. Geim and K. S. Novoselov, Nat. Mater. **6**, 183 (2007).

[3] A. H. Castro Neto, F. Guinea, N. M. R. Peres, K. S. Novoselov, and A. K. Geim, Rev. Mod. Phys. **81**, 109 (2009).

[4] S. Das Sarma, S. Adam, E. H. Hwang, and E. Rossi, Rev. Mod. Phys. **83**, 407 (2011).

[5] M. I. Katsnelson, Mater. Today **10**, 20 (2007).

[6] P. Avouris, Z. H. Chen, and V. Perebeinos, Nat. Nanotechnol. **2**, 605 (2007).

[7] S. Y. Zhou, G.-H. Gweon, A. V. Fedorov, P. N. First, W. A. der Heer, D.-H. Lee, F. Guinea, A. H. Castro Neto, and A. Lanzara, Nat. Mater. **6**, 770 (2007).

[8] K. Wakabayashi, K. Sasaki, T. Nakanishi, and T. Enoki, Sci. Technol. Adv. Mater. **11**, 054504 (2010).

[9] J. J. Palacios, J. F. Rossier, L. Brey, and H. A. Fertig, Semicond. Sci. Technol. **25**, 033003 (2010).

[10] L. Pisani, J. A. Chan, B. Montanari, and N. M. Harrison, Phys. Rev. B **75**, 064418 (2007).

[11] L. Yang, C. H. Park, Y.-W. Son, M. L. Cohen, and S. G. Louie, Phys. Rev. Lett. **99**, 186801 (2007).

[12] H. Hiura, Appl. Surf. Sci. **222**, 374 (2004).

[13] K. S. Novoselov, A. K. Geim, S. V. Morozov, D. Jiang, M. I. Katsnelson, I. V. Grigorieva, S. V. Dubonos, and A. A. Firsov, Nature (London) **438**, 197 (2005).

[14] Y. Zhang, Y. W. Tan, H. L. Stormer, and P. Kim, Nature (London) **438**, 201 (2005).

[15] K. Nakada, M. Fujita, G. Dresselhaus, and M. S. Dresselhaus, Phys. Rev. B **54**, 17954 (1996).

[16] B. Özyilmaz, P. Jarillo-Herrero, D. Efetov, D. A. Abanin, L. S. Levitov, and P. Kim, Phys. Rev. Lett. **99**, 166804 (2007).

[17] M. Y. Han, B. Özyilmaz, Y. Zhang, and P. Kim, Phys. Rev. Lett. **98**, 206805 (2007).

[18] M. Fujita, K. Wakabayashi, K. Nakada, and K. Kusakabe, J. Phys. Soc. Jpn. **65**, 1920 (1996).

[19] L. Brey and H. A. Fertig, Phys. Rev. B **73**, 235411 (2006).

[20] Y. Niimi, T. Matsui, H. Kambara, K. Tagami, M. Tsukada, and H. Fukuyama, Phys. Rev. B **73**, 085421 (2006).

[21] Y. Kobayashi, K. I. Fukui, T. Enoki, and K. Kusakabe, Phys. Rev. B **73**, 125415 (2006).

[22] Y.-W. Son, M. L. Cohen, and S. G. Louie, Nature (London) **444**, 347 (2006).

[23] F. Wu, E. Kan, H. Xiang, S.-H. Wei, M.-H. Whangbo, and J. Yang, Appl. Phys. Lett. **94**, 223105 (2009).

[24] C. Tao, L. Jiao, O. V. Yazyev, Y.-C. Chen, J. Feng, X. Zhang, R. B. Capaz, J. M. Tour, A. Zettl, S. G. Louie, H. Dai, and M. F. Crommie, Nat. Phys. **7**, 616 (2011).

[25] Y.-W. Son, M. L. Cohen, and S. G. Louie, Phys. Rev. Lett. **97**, 216803 (2006).

[26] J. Kunstmann, C. Özdogan, A. Quandt, and H. Fehske, Phys. Rev. B **83**, 045414 (2011).

[27] E. Kan, Z. Li, and J. Yang, Nano **03**, 433 (2008).

[28] N. Tombros, C. Jozsa, M. Popinciuc, H. T. Jonkman, and B. J. van Wees, Nature (London) **448**, 571 (2007).

[29] Y. Seo and W. Jhe, Rep. Prog. Phys. **71**, 016101 (2008).

[30] L. Gross, F. Mohn, N. Moll, B. Schuler, A. Criado, E. Guitián, D. Peña, A. Gourdon, and G. Meyer, Science **337**, 1326 (2012).

[31] E. Kan, H. Xiang, J. L. Yang, and J. G. Hou, J. Chem. Phys. **127**, 164706 (2007).

[32] R. C. Longo, J. Carrete, J. Ferrer, and L. J. Gallego, Phys. Rev. B **81**, 115418 (2010).

[33] S. R. Power, V. M. de Menezes, S. B. Fagan, and M. S. Ferreira, Phys. Rev. B **84**, 195431 (2011).

[34] H. Sevinçli, M. Topsakal, E. Durgun, and S. Ciraci, Phys. Rev. B **77**, 195434 (2008).

[35] V. A. Rigo, T. B. Martins, A. J. R. da Silva, A. Fazzio, and R. H. Miwa, Phys. Rev. B **79**, 075435 (2009).

[36] C. Cocchi, D. Prezzi, A. Calzolari, and E. Molinari, J. Chem. Phys. **133**, 124703 (2010).

[37] P. O. Lehtinen, A. S. Foster, Y. Ma, A. V. Krasheninnikov, and R. M. Nieminen, Phys. Rev. Lett. **93**, 187202 (2004).

[38] J. J. Palacios, J. Fernández-Rossier, and L. Brey, Phys. Rev. B **77**, 195428 (2008).

[39] J.-H. Chen, L. Li, W. G. Cullen, E. D. Williams, and M. S. Fuhrer, Nat. Phys. **7**, 535 (2011).

[40] L. S. Mattos, Ph.D. thesis, Stanford University, 2009; L. S. Mattos, C. R. Moon, P. B. van Stockum, J. C. Randel, H. C. Manoharan, M. W. Sprinkle, C. Berger, W. A. de Heer, K. Sengupta, and A. V. Balatsky, APS March Meeting, Abstract No. T25.009, 2009.

[41] V. Madhavan, W. Chen, T. Jamneala, M. F. Crommie, and N. S. Wingreen, Phys. Rev. B **64**, 165412 (2001).

[42] S.-P. Chao and V. Aji, Phys. Rev. B **83**, 165449 (2011).

[43] B. Uchoa, T. G. Rappoport, and A. H. Castro Neto, Phys. Rev. Lett. **106**, 016801 (2011).

[44] M. Vojta, L. Fritz, and R. Bulla, Europhys. Lett. **90**, 27006 (2010).

[45] Z. G. Zhu, K. H. Ding, and J. Berakdar, Europhys. Lett. **90**, 67001 (2010).

[46] T. O. Wehling, A. V. Balatsky, M. I. Katsnelson, A. I. Lichtenstein, and A. Rosch, Phys. Rev. B **81**, 115427 (2010).

[47] D. Jacob and G. Kotliar, Phys. Rev. B **82**, 085423 (2010).

[48] A. C. Hewson, *Kondo Problem to Heavy Fermions* (Cambridge University Press, Cambridge, 1993).

[49] G. Kotliar and A. E. Ruckenstein, Phys. Rev. Lett. **57**, 1362 (1986).

[50] B. Dong and X. L. Lei, Phys. Rev. B **66**, 113310 (2002).

[51] C. Lacroix, J. Phys. F: Met. Phys. **11**, 2389 (1981).

[52] O. Entin-Wohlman, A. Aharony, and Y. Meir, Phys. Rev. B **71**, 035333 (2005).

[53] V. Kashcheyevs, A. Aharony, and O. Entin-Wohlman, Phys. Rev. B **73**, 125338 (2006).

[54] N. S. Wingreen and Y. Meir, Phys. Rev. B **49**, 11040 (1994).

[55] N. E. Bickers, D. L. Cox, and J. W. Wilkins, Phys. Rev. B **36**, 2036 (1987).
[56] Y. Kuramoto, Z. Phys. B **53**, 37 (1983).
[57] Th. Pruschke and N. Grewe, Z. Phys. B **74**, 439 (1989).
[58] N. Grewe, T. Jabben, and S. Schmitt, Eur. Phys. J. B **68**, 23 (2009).
[59] K. Haule, S. Kirchner, J. Kroha, and P. Wölfle, Phys. Rev B **64**, 155111 (2001).
[60] D. Gerace, E. Pavarini, and L. C. Andreani, Phys. Rev. B **65**, 155331 (2002).
[61] P. Hohenberg and W. Kohn, Phys. Rev. **136**, B864 (1964).
[62] J. P. Perdew, K. Burke, and M. Ernzerhof, Phys. Rev. Lett. **77**, 3865 (1996).
[63] J. Heyd, G. E. Scuseria, and M. Ernzerhof, J. Chem. Phys. **118**, 8207 (2003).
[64] J. Paier, M. Marsman, K. Hummer, G. Kresse, I. C. Gerber, and J. G. Ángyán, J. Chem. Phys. **124**, 154709 (2006).
[65] R. Gillen and J. Robertson, Phys. Status Solidi B **247**, 2945 (2010).
[66] H. Xiao, J. Tahir-Kheli, and W. A. Goddard, J. Phys. Chem. Lett. **2**, 212 (2011).
[67] S. Park, B. Lee, S. H. Jeon, and S. Han, Curr. Appl. Phys. **11**, S337 (2011).
[68] V. Barone, O. Hod, J. E. Peralta, and G. E. Scuseria, Acc. Chem. Res. **44**, 269 (2011).
[69] E.-J. Kan, Z. Li, J. Yang, and J. G. Hou, Appl. Phys. Lett. **91**, 243116 (2007).
[70] G. Kresse and J. Furthmüller, Phys. Rev. B **54**, 11169 (1996).
[71] P. E. Blöchl, Phys. Rev. B **50**, 17953 (1994); G. Kresse and D. Joubert, *ibid.* **59**, 1758 (1999).
[72] T. Ozaki, Phys. Rev. B **67**, 155108 (2003); T. Ozaki and H. Kino, *ibid.* **69**, 195113 (2004); J. Chem. Phys. **121**, 10879 (2004).
[73] K. T. Chan, J. B. Neaton, and M. L. Cohen, Phys. Rev. B **77**, 235430 (2008).
[74] A. I. Liechtenstein, V. I. Anisimov, and J. Zaanen, Phys. Rev. B **52**, R5467 (1995).
[75] E. H. Lieb, Phys. Rev. Lett. **62**, 1201 (1989).
[76] H. Xiang, E. Kan, S. H. Wei, M. H. Whangbo, and J. Yang, Nano Lett. **9**, 4025 (2009).
[77] S. Kümmel and L. Kronik, Rev. Mod. Phys. **80**, 3 (2008).
[78] G. Cantele, Y. S. Lee, D. Ninno, and N. Marzari, Nano Lett. **9**, 3425 (2009).
[79] D. Jiang, X. Q. Chen, W. Luo, and W. A. Shelton, Chem. Phys. Lett. **483**, 120 (2009).
[80] T. B. Martins, R. H. Miwa, A. J. R. da Silva, and A. Fazzio, Phys. Rev. Lett. **98**, 196803 (2007).
[81] L. Sun, P. Wei, J. Wei, S. Sanvito, and S. Hou, J. Phys.: Condens. Matter **23**, 425301 (2011).
[82] X. H. Zheng, X. L. Wang, L. F. Huang, H. Hao, J. Lan, and Z. Zeng, Phys. Rev. B **86**, 081408(R) (2012).
[83] T. Pruschke and R. Bulla, Eur. Phys. J. B **44**, 217 (2005).
[84] A. Makarovski, L. An, J. Liu, and G. Finkelstein, Phys. Rev. B **74**, 155431 (2006).
[85] B. R. Bułka and S. Lipiński, Phys. Rev. B **67**, 024404 (2003).
[86] J. S. Lim, M. S. Choi, M. Y. Choi, R. Lopez, and R. Aguado, Phys. Rev. B **74**, 205119 (2006).
[87] S. Lipiński and D. Krychowski, Phys. Rev. B **81**, 115327 (2010).
[88] P. Trocha, Phys. Rev. B **82**, 125323 (2010).
[89] A. N. Rudenko, F. J. Keil, M. I. Katsnelson, and A. I. Lichtenstein, Phys. Rev. B **86**, 075422 (2012).
[90] A. K. Zhuravlev and V. Yu. Irkhin, Phys. Rev. B **84**, 245111 (2011).
[91] V. Yu Irkhin, J. Phys.: Condens. Matter **23**, 065602 (2011).
[92] A. C. Seridonio, F. M. Souza, and I. A. Shelykh, J. Phys.: Condens. Matter **21**, 0953003 (2009).
[93] M. Vojta and R. Bulla, Phys. Rev. B **65**, 014511 (2001).
[94] R. Korytar, M. Pruneda, J. Junquera, P. Ordejon, and N. Lorente, J. Phys.: Condens. Matter **22**, 385601 (2010).
[95] M. Karolak, T. O. Wehling, F. Lechermann, and A. I. Lichtenstein, J. Phys.: Condens. Matter **23**, 085601 (2011).
[96] S. W. Hla, J. Vac. Sci. Technol. B **23**, 1351 (2005).
[97] T. Jamneala, V. Madhavan, W. Chen, and M. F. Crommie, Phys. Rev. B **61**, 9990 (2000).
[98] K. Nagaoka, T. Jamneala, M. Grobis, and M. F. Crommie, Phys. Rev. Lett. **88**, 077205 (2002).
[99] N. Knorr, M. A. Schneider, L. Diekhöner, P. Wahl, and K. Kern, Phys. Rev. Lett. **88**, 096804 (2002).
[100] D. Rugar, R. Budakian, H. J. Mamin, and B. W. Chui, Nature (London) **430**, 329 (2004).
[101] H-S. Goan and T. A. Brun, Proc. SPIE **5276**, 250 (2004).
[102] Y. Mao, J. Yuan, and J. Zhong, J. Phys.: Condens. Matter **20**, 115209 (2008).
[103] H. Valencia, A. Gil, and G. Frapper, J. Phys. Chem. C **114**, 14141 (2010).
[104] T. O. Wehling, A. I. Lichtenstein, and M. I. Katsnelson, Phys. Rev. B **84**, 235110 (2011).
[105] E. Kan, Z. Li, and J. Yang, *Graphene Nanoribbons: Geometric, Electronic, and Magnetic Properties* (InTech, Rijeka, Croatia, 2011).